ACS APPLIED BIO MATERIALS Cite This: ACS Appl. Bio Mater. 2019, 2, 2192−2201 Article www.acsabm.org

Linker-Mediated Assembly of Virus-Like Particles into Ordered Arrays via Electrostatic Control

Nicholas E. Brunk,*,†,⊥ Masaki Uchida,*,‡,⊥ Byeongdu Lee,*,¶ Masafumi Fukuto,*,§,∥ Lin Yang,*,§ Trevor Douglas,*,‡ and Vikram Jadhao*,†

†Intelligent Systems Engineering, Indiana University, Bloomington, Indiana 47408, United States

‡Department of Chemistry, Indiana University, Bloomington, Indiana 47405, United States

¶X-Ray Science Division, Advanced Photon Source, Argonne National Laboratory, 9700 South Cass Avenue, Lemont, Illinois 60439, United States

§National Synchrotron Light Source II, Brookhaven National Laboratory, Upton, New York 11973, United States

∥Condensed Matter Physics and Materials Science Department, Brookhaven National Laboratory, Upton, New York 11973, United States

Supporting Information

ABSTRACT: Nanoscale virus-like particles (VLPs), which are self-assembled from protein subunits, offer the possibility of generating hierarchically assembled functional materials such as biomimetic catalytic systems and optical metamaterials. We explore the capacity to control and tune a higher-order assembly of VLPs into ordered array materials over a wide range of ionic conditions using a combination of experimental and computational methods. The integrated methodology demonstrates that P22 VLP variants, genetically engineered to exhibit different surface charges, self-assemble into ordered arrays in the presence of PAMAM dendrimers acting as oppositely charged, macromolecular linkers. Ordered assembly occurs at an optimal ionic strength that strongly correlates with the VLP surface charge. The ordered VLP arrays exhibit the same long-range order and a similar configuration of VLP-bound dendrimers, regardless of the VLP surface charge. The experimentally validated model identifies key electrostatic and kinetic mechanisms underlying the self-assembly process and guides the modulation of dendrimer concentration as a control parameter to tune the assembly of VLPs. The integrated approach opens new design and control strategies to fabricate active functional materials via the self-assembly of engineered VLPs.

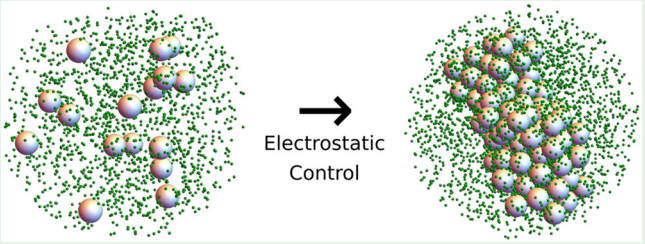

KEYWORDS: *self-assembly, virus-like particles, electrostatic control, ordered arrays, biomimetic materials, kinetic control, molecular dynamics simulations*

INTRODUCTION

Biological materials are often generated via the process of self-assembly. There is a growing interest in bioinspired approaches to the fabrication of functional synthetic materials via the spontaneous self-assembly of nanoscale, biomimetic building blocks.[1−12] For example, gold nanoparticles (NPs) conjugated with DNA have been shown to self-assemble into three-dimensional crystalline nanostructures that exhibit emergent properties with potential technological applications in plasmonics and medical diagnostics.[6,13−16] Similarly, virus-like particles (VLPs) have been used as templates for nanomaterial synthesis and as building blocks for superlattice materials due to their high monodispersity and ability to encapsulate a wide range of cargo molecules including active enzymes and inorganic NPs.[10,12,17] In this study, we explore the capacity to control and tune the higher-order assembly of VLPs into ordered arrays over a wide range of ionic conditions using a combination of experimental and computational methods.

The assembly of individual VLPs, which encapsulate multiple copies of an enzyme, into an ordered lattice effectively increases the concentration of the catalytically active particles by several hundred-fold, leading to a highly efficient catalytic turnover that enables the recovery and reuse of the materials.[12,18] The hierarchical assembly is highly dependent on the nature of the VLP exterior but is independent of the encapsulated cargo. A vast range of catalytic cargos can be incorporated into individual VLPs, which when assembled hierarchically into a lattice creates the possibility for fabricating materials that can facilitate complex coupled catalytic transformations. In addition to forming catalytic materials, a controlled assembly of VLPs into ordered lattices can lead to the development of metamaterials whose electromagnetic properties are dictated by the organization of their

Received: February 26, 2019
Accepted: April 22, 2019
Published: April 22, 2019

   DOI: 10.1021/acsabm.9b00166
ACS Appl. Bio Mater. 2019, 2, 2192−2201

structures.[19,20] Understanding the mechanisms involved in the higher-order assembly of VLPs is thus critical for the development of these new materials.

There have been several experimental advances in generating self-assembled, higher-order structures using icosahedral VLPs and linkers.[10,12,21,22] For example, ordered arrays were formed using bacteriophage P22 VLPs and Generation 6 (G6) polyamidoamine (PAMAM) dendrimers as linkers,[12,18] and superlattices were observed for smaller Cowpea chlorotic mottle VLPs using gold NPs and charged dendrimers as linkers.[10,22] Recently, similar lattices were assembled using Simian Virus 40 as building blocks with magnesium ions providing the electrostatic control.[21] Despite the significant experimental interest in higher-order assembly phenomena associated with the VLP-linker systems, there is a lack of computational studies aimed at understanding assembly mechanisms in these systems. Simulations can isolate the factors determining the thermodynamically favored structures resulting from the self-assembly of nanoscale building blocks, and can expedite the search for conditions where such structures are readily realized.[2,4,16,23−26] Molecular dynamics simulations characterized the hybridization processes that enabled the crystallization of spherical, gold NPs 8−15 nm in diameter using DNA as linkers.[6,24] Numerical studies probed the difficulty of achieving crystalline structures using oppositely charged NPs with different average sizes (in the 1−10 nm size range).[25,27] At the microscale, coarse-grained simulations of the assembly of oppositely charged colloids yielded critical information on the formation of stable binary structures, enabling the experimental realization of colloidal crystals.[28−30]

We recently demonstrated experimentally that genetically modified P22 VLPs (P22-E2) spontaneously assemble into ordered arrays in the presence of oppositely charged linkers (PAMAM G6 dendrimers) with a long-range order in sharp contrast to similarly charged wild-type P22 viruses (wtP22) that exhibit aggregation but no long-range order.[12] The differences in assembly behavior between wtP22 and P22-E2 were attributed to steric effects arising from the peptide engineered on the capsid surface. In this study, we integrate computational and experimental methods to systematically explore the materials design space for identifying the key mechanisms governing the assembly of genetically modified virus building blocks into ordered array materials. Genetic engineering via the addition of peptides is employed to tune the surface charge of the P22 VLP to produce new VLP variants (P22-K2, P22-Q2). A coarse-grained model of the VLP-linker system is developed and simulated using molecular dynamics (MD) with the initial application to investigate, in combination with experimental methods, the self-assembly of modified P22 VLPs mediated by PAMAM dendrimers. We demonstrate that the ordered assembly in the P22 VLP-PAMAM dendrimer system can be realized and controlled by tuning the surface charge of the capsid, and we establish both electrostatic and kinetic control mechanisms underlying the self-assembly process.

The capsid variants with different surface charges lead to very different ionic strength thresholds I_t, above which they do not assemble into arrays, exhibiting a correlation between the surface charge and ionic strength threshold. We note that an experimental system has not been reported in the literature where the surface charge of a capsid has been systematically changed, without disrupting the capsid structure, and the associated higher-order assembly behavior demonstrated across a wide range of ionic strength conditions.

Simulations establish the ratio of condensed dendrimers (i.e., dendrimers that are bound to the P22 VLP surface) and bridging dendrimers (i.e., condensed dendrimers shared between multiple VLPs) as the key parameter that dictates the order of assembly. The ratio of bridging to condensed dendrimers is maximized at the ionic strength threshold regardless of the surface charge of capsid variants to yield the long-range order not achieved at other ionic strengths. This information explicitly demonstrates the importance of the optimal density of linker-mediated bridges in generating virus-based lattices. Simulations provide new information on the kinetics of the virus linker bridge formation during the assembly process, establishing the concentration of PAMAM dendrimers as a control parameter to generate the optimal PAMAM-virus attraction and enhance the higher-order assembly capacity at very low ionic strengths. For the first time, simulations show that the lack of assembly at a low ionic strength observed in previous experiments on P22-E2 VLPs[12] is due to an excessive linker concentration; new experiments validate this claim.

The experimental and computational investigations reveal the links between VLP-linker characteristics, solution conditions, and self-assembled higher-order structures. These links illustrate how the assembly of P22 VLPs into ordered materials can be controlled by changing the VLP surface charge and how the assembly can be regulated by exploiting kinetic effects. This is the first comprehensive study of VLP-linker systems using a combination of experiments and simulations that demonstrates the success of a simulation-experiment feedback loop to understand and improve the process of producing higher-order assemblies of virus-based materials. The integrated methodology opens new design and control strategies that expand and expedite investigations of higher-order assemblies involving different VLP-linker systems and other soft-matter-based NPs.[10,11,21,22,31]

MATERIALS AND COMPUTATIONAL MODEL

Synthesis of Charge-Tunable P22 VLPs. To experimentally study the self-assembly of VLPs into higher-order structures controlled by the VLP surface charge, three types of P22 VLP variants possessing different surface charges were prepared by genetic engineering of the P22 coat protein (CP). The three variants, P22-E2, P22-Q2, and P22-K2, formed a cage-like structure with the same diameter of ≈56 nm (Figures S1−S3), but exhibited different surface charges characterized with ζ potential values of −30.4, −23.6, and −12.8 mV, respectively, at an ionic strength of 41.1 mM (Figure S4). Reliable measurements of the ζ potential at higher ionic strengths were not possible due to instrument limitations. The surface charge of P22-E2 was nearly the same as that of wtP22 (−30.7 mV). A higher-order assembly of each VLP variant mediated by the oppositely charged Generation 6 PAMAM dendrimers (G6 dendrimers) was investigated in a range of ionic strength solutions. The array formation was evaluated by measuring the turbidity of the mixed solution using UV−vis spectroscopy. The mean hydrodynamic size of the assembled arrays was estimated by dynamic light scattering (DLS). The long-range structure of the assembled arrays was assessed with small-angle X-ray scattering (SAXS). Detailed experimental methods, characterization of engineered VLPs, and analysis of assembled arrays are provided in the Supporting Information.

Coarse-Grained Model of VLP-Linker Systems. P22 VLPs are charged, hollow nanostructures and are significantly larger than the linkers employed to engineer their higher-order assembly. Probing the assembly of these large-sized (diameter ≈ 50 nm) VLPs using

DOI: 10.1021/acsabm.9b00166
ACS Appl. Bio Mater. 2019, 2, 2192−2201

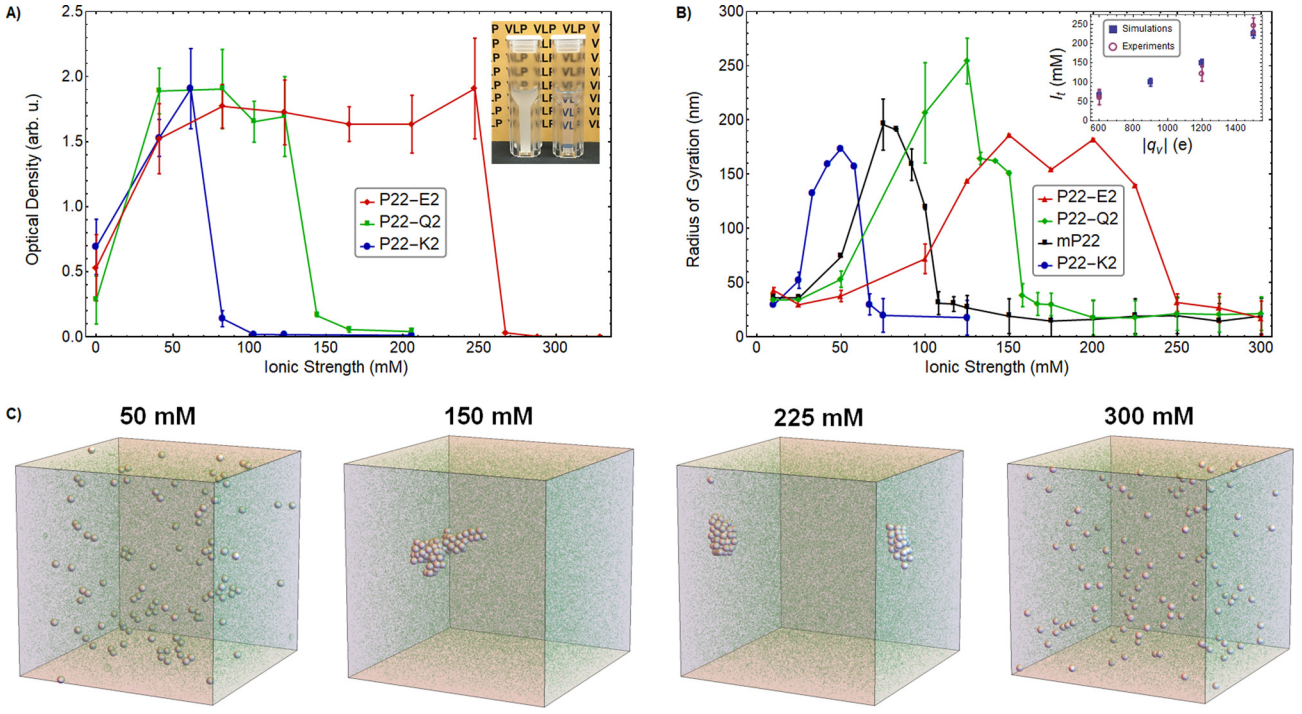

Figure 1. Assembly of P22 VLPs mediated by G6 dendrimers as a function of the ionic strength (I) in experiments (A) and simulations (B and C). (A) Optical density at λ = 800 nm. The ionic strength threshold I_t and range over which significant assembly is observed are a function of the VLP surface charge. P22-E2 (red) has the highest surface charge and exhibits a larger I_t, followed by P22-Q2 (green) and P22-K2 (blue). (Inset) Solution of P22-E2 mixed with G6 at I = 206 mM became turbid due to the formation of large aggregates (left), whereas those mixed at I = 329 mM remained clear (right). (B) Mean radius of gyration R_g of the largest cluster of P22 VLPs obtained from simulations of the VLP−dendrimer systems for P22-E2 (red), P22-Q2 (green), P22-K2 (blue), and a model VLP mP22 (black). I_t and range of ionic strengths over which significant bulk assembly occurs change with the VLP surface charge and correlate well with experiments (Inset). (C) Selected simulation snapshots of typical steady-state configurations of the assembly of P22-E2 VLPs (silver spheres) in the presence of smaller dendrimers (green spheres) as a function of ionic strength, I. A transition from a nonassembled configuration to an ordered array of VLPs is observed as I is lowered below $I_t \approx 225$ mM. Bulk assembly continues to occur albeit with reduced order as I is lowered further, but is significantly suppressed for $I \lesssim 50$ mM.

atomistic models becomes prohibitively expensive due to the large number of VLPs and linkers needed to investigate the experimentally realized structures. Coarse-grained models with sufficient physical detail to capture the relevant competing interactions offer a feasible alternative.

To investigate the G6 dendrimer-mediated aggregation of P22 VLPs, a coarse-grained model of the VLP−dendrimer system was developed. The model was inspired by coarse-grained models employed to study the assembly of systems involving oppositely charged particles with different average sizes.[25,27,28,32] P22 VLPs were modeled as uniformly charged, spherical shells. Peptide-bound variants of P22 (P22-E2, P22-Q2, P22-K2) were assigned the same mass, m_v = 20 MDa, and diameter, σ_v = 56 nm, consistent with the DLS data (see Figures S1−S3). G6 dendrimers were modeled as uniformly charged spheres with a mass of m_d = 0.058 MDa and a diameter of σ_d = 6.7 nm.

A combination of experimentally informed analytical approximations,[33] available estimates,[34,35] and a simulation data-driven approach was employed to select the model parameters characterizing the effective surface charge of the VLP and dendrimer. The VLP surface charge q_v was chosen to scale linearly with experimentally measured values of ζ and varied between $-1500e$ (for P22-E2 with $\zeta \approx 30$ mV at 41.1 mM) and $-600e$ (for P22-K2 with $\zeta \approx -12$ mV at 41.1 mM). The dendrimer surface charge parameter q_d was set to $35e$; this value was consistent with available estimates in the literature on PAMAM dendrimers.[35] Details are provided in the Supporting Information.

The electrostatic interactions between each pair (i,j) of spherical particles separated by a (center-to-center) distance $r_{ij} = r$ were modeled using the standard Yukawa potential:

$$u_E(r) = \frac{q_i q_j e^{\kappa(\sigma_i/2+\sigma_j/2)}}{(1+\kappa\sigma_i/2)(1+\kappa\sigma_j/2)} \frac{l_B e^{-\kappa r}}{r} \quad (1)$$

where u_E is measured in units of k_BT and q_i is the net surface charge parameter measured in units of the electronic charge e. $l_B = e^2/(4\pi\epsilon_0\epsilon_w k_B T) \approx 0.7$ nm is the Bjerrum length in water at temperature T = 298 K, where ϵ_0 is the permittivity of the vacuum and ϵ_w = 78.5 is the dielectric constant of water. $\kappa = \lambda_D^{-1} = \sqrt{8\pi l_B I}$ is the inverse of the screening (Debye) length λ_D, where I is the ionic strength of the solution. I was swept from 10 to 300 mM, changing λ_D from 3.04 to 0.514 nm.

The steric interactions for each pair of particles were modeled using the modified Lennard-Jones (LJ) potential to account for significant differences in the size of the particles:[32]

$$u_{LJ}(r) = 1 + 4\left(\left(\frac{\sigma_{hc}}{r-\Delta_{ij}}\right)^{12} - \left(\frac{\sigma_{hc}}{r-\Delta_{ij}}\right)^{6}\right) \quad (2)$$

for $\Delta_{ij} < r < \sqrt[6]{2}\sigma_{hc} + \Delta_{ij}$, where u_{LJ} is measured in units of k_BT. For $r \le \Delta_{ij}$, $u_{LJ}(r) = \infty$, and for $r \ge \sqrt[6]{2}\sigma_{hc} + \Delta_{ij}$, $u_{LJ}(r) = 0$. The characteristic LJ energy scale was chosen to be k_BT, and $\Delta_{ij} = (\sigma_i + \sigma_j)/2 - \sigma_{hc}$. The parameter σ_{hc} plays the role of the VLP surface accessibility to incoming dendrimers and models the effective VLP−dendrimer steric interaction (see Supporting Information for details). For all 3 VLP variants, σ_{hc} was chosen to be 6.7 nm to allow for an average VLP−dendrimer closest approach distance of ≈30.7 nm, which is ≈0.6 nm smaller than the VLP−dendrimer touching distance. This value for the VLP−dendrimer closest approach distance is in agreement with previously reported SAXS-based

DOI: 10.1021/acsabm.9b00166
ACS Appl. Bio Mater. 2019, 2, 2192−2201

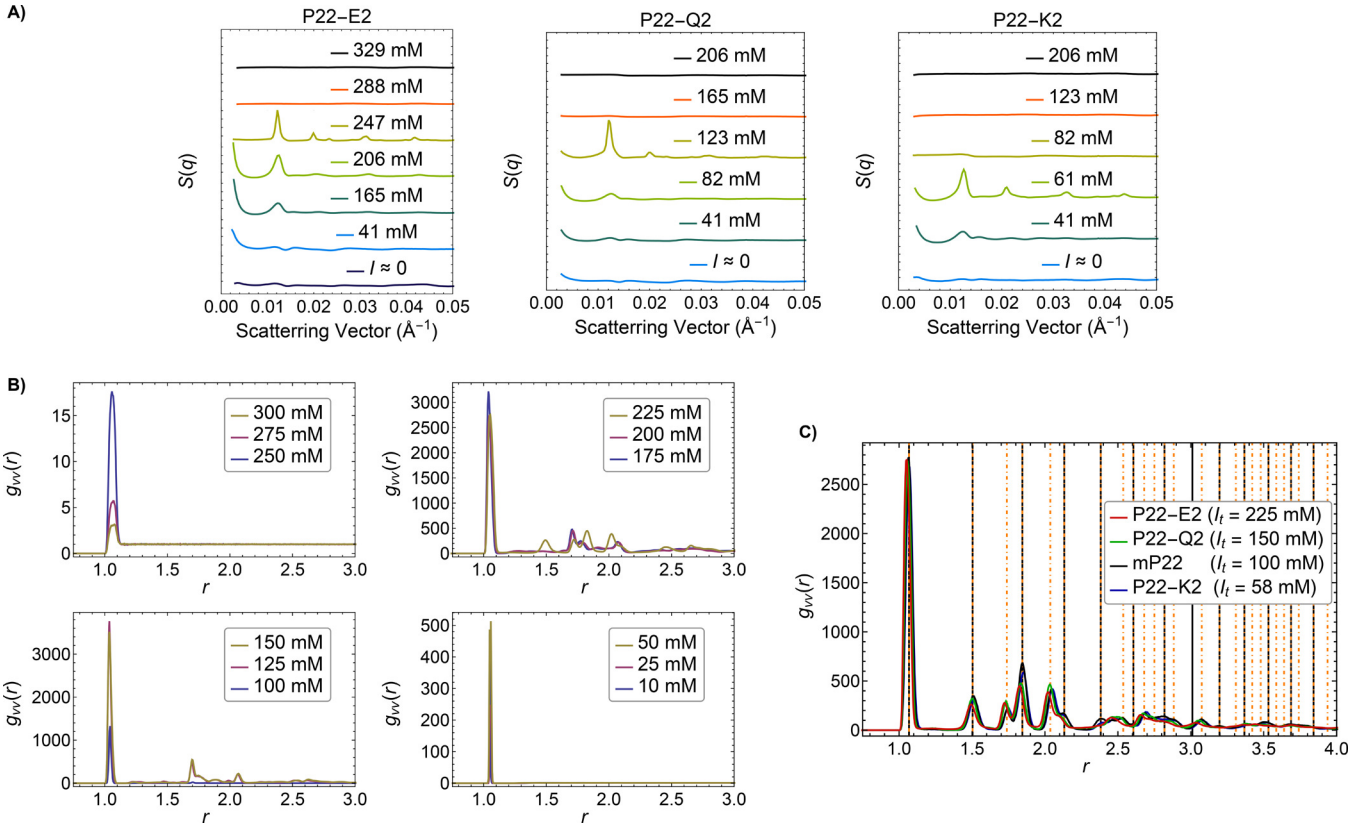

Figure 2. Analysis of structures formed in experiments (A) and simulations (B and C). (A) Structure factors $S(q)$ from SAXS for P22-E2, P22-Q2, and P22-K2 systems. For all VLP variants, an increase in the long-range order (indicated by the number of peaks in $S(q)$) is observed as the ionic strength threshold I_t is achieved. $S(q)$ is shown with a vertical offset between experiments at different ionic strengths for clarity. (B) VLP–VLP pair correlation functions (PCFs), $g_{vv}(r)$, from simulations for P22-E2 VLPs at different ionic strength (I) values (including the values associated with the snapshots in Figure 1C and Figure S7). The plots indicate the extent of bulk assembly and long-range order. As in the experiment, the most ordered structure, distinct from those produced at other I, occurs at $I_t \approx 225$ mM. (C) PCF for each VLP charge variant at its corresponding I_t; the latter changes with the VLP surface charge, in good agreement with experiments (A) and is given in the legend. Black vertical lines correspond to the peak positions of a face-centered cubic (FCC) lattice; orange dot-dashed lines correspond to peak positions of a hexagonal close-packed (HCP) lattice. All PCFs collapse to the same curve, indicating each VLP system self-organizes into the same structure at I_t. PCFs and $S(q)$ characterizing the ordered domains within the assembled array at threshold match well with FCC structure; additional peaks corresponding to HCP lattice are observed in simulated systems and in some experimental samples (Figure S11).[12]

experimental assessments[12] of the average nearest-neighbor spacing of 61.5 nm between two P22-E2 VLPs bridged by an interstitial dendrimer in an ordered array (reduced from the touching distance with bridging of 62.7 nm). Figure S5 (red curve) shows the net P22-E2 VLP–dendrimer interaction potential ($u_{net} = u_E + u_{LJ}$) with σ_{hc} = 6.7 nm at an ionic strength of 225 mM.

Molecular Dynamics Simulations. Each system was simulated using MD in an NVT ensemble within a periodic, cubic box. A Nosé–Hoover thermostat was used to simulate the system at a fixed temperature of T = 298 K. Simulations ran for at least ≈0.5–1 ms; most simulations where aggregates were observed required ≈0.5 ms to reach a steady state. An extensive exploration of the parameter space was performed (e.g., $q_v = -600e$ to $-1500\,e$, I = 10–300 mM; $c_d = 25c_v$ to $1000c_v$), yielding data from over 100 simulations. Simulation methods are discussed in detail in the Supporting Information.

RESULTS AND DISCUSSION

Dendrimer-Mediated Assembly of P22 VLPs. Solutions of P22-E2, P22-Q2, and P22-K2 VLP variants were prepared at a concentration of c_v = 37 nM (packing fraction ≈ 0.002) with the G6 PAMAM dendrimer concentration at $c_d = 1000c_v$. For a range of ionic strengths, I, a high optical density in turbidity measurements of the sample solutions using UV–vis spectroscopy (Figure 1A) and DLS measurements (Figure S6) was observed. Over a similar range of I, clusters exhibiting a large radius of gyration were observed in MD simulations (Figure 1B), indicating the formation of large aggregates (Figure 1C, Figures S7–S9). Conversely, almost 0 optical density in experiments and clusters with a low radius of gyration ($\approx \sigma_v/2$) in simulations were indicative of no significant higher-order assembly.

The ionic strength above which no significant assembly occurs (defined as the ionic strength threshold I_t) changed for each variant. In both simulations and experiments, VLPs with less surface charge exhibited a lower I_t (inset in Figure 1); in other words, weakly charged systems required a longer Debye length λ_D (weakly screened interactions) to form large aggregates. Simulations found the assembly thresholds for P22-E2, P22-Q2, and P22-K2 to be I_t = 225 mM (Figure 1C and Figure S7), I_t = 150 mM (Figure S8), and I_t = 58 mM (Figure S9), respectively; these values were in good agreement with experimental values of I_t = 247 mM, I_t = 123 mM, and I_t = 61.7 mM, respectively. Threshold estimates in experiments for each VLP variant were made based on change in the turbidity of the VLP solution when mixed with dendrimer solution at different ionic strengths (Figure 1A; see details in the

DOI: 10.1021/acsabm.9b00166
ACS Appl. Bio Mater. 2019, 2, 2192–2201

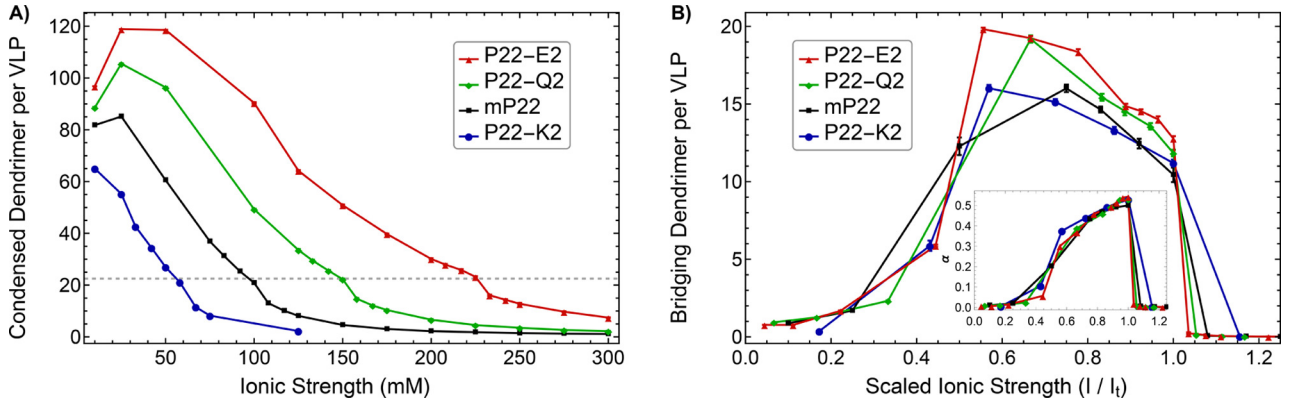

Figure 3. VLP-bound dendrimer distributions from simulations of the higher-order self-assembly of different VLP variants including the model VLP mP22. (A) The average number of condensed dendrimers per VLP (N_c) vs ionic strength, I. The onset of assembly for P22-E2, P22-Q2, mP22, and P22-K2 occurs at I_t = 225, 150, 100, and 58 mM, respectively. Each VLP system at their corresponding I_t exhibits a similar number of condensed dendrimers per VLP, $N_c \approx 24$, highlighted by the dashed line. (B) The average number of bridging dendrimers N_b per VLP vs ionic strength scaled by the ionic strength threshold (I/I_t). (Inset) Variation of the ratio N_b/N_c vs I/I_t. For all VLPs, this ratio is maximized at I_t when the assembled structure is an ordered array with the highest long-range order.

Supporting Information). For example, a higher-order assembly of four samples of P22-E2 were examined at I = 206, 247, 267, and 288 mM. All four samples showed a dramatic increase in the optical density at both I = 206 and 247 mM, while showing no significant increase for $I \geq 267$ mM. Accordingly, I_t of P22-E2 was defined as 247 mM. Reported experimental threshold values are thus accurate up to the ionic strength increment of ≈20 mM. An additional model VLP (mP22), with a charge between P22-Q2 and P22-K2, was investigated in simulations and its threshold for assembly was found to be at I_t = 100 mM.

The onset of assembly was abrupt in both simulations and experiments, with simulations showing the transition occurs with a change in I less than 10 mM; P22-E2 VLPs assembled into arrays at I_t = 225 mM, while no assembly was observed at I = 233 mM. In experiments, P22 VLPs assembled to micrometer-sized aggregates below I_t except at I = 0 mM, where the size of the assembly was recorded to be a few hundred nanometers. Simulations found smaller aggregate sizes within the assembly regime; this difference can be attributed to finite size effects in simulations. At a very low I ($\ll I_t$), deviations between simulations and experiments were observed. Simulations found no significant assembly, while experiments still observed smaller aggregates, albeit with a greatly reduced long-range order (Figure 2A).

SAXS Measurements and Pair Correlation Functions. All three variants exhibited sharp SAXS peaks at the same scattering vector (q) when they were assembled near their threshold ionic strength ($I_t \approx$ 247 mM for P22-E2, 123 mM for P22-Q2, and 61.7 mM for P22-K2), suggesting that they form arrays with a similar structure (Figure 2A). A similar long-range order at I_t characterized by sharp peaks in pair correlation functions (PCF) computed using VLP trajectory data was also observed in simulations of all three P22 VLP variants (Figure 2B, Figure 2C, and Figure S10). Both PCFs and SAXS scattering profiles matched well with a face-centered cubic (FCC) structure with a nearest-neighbor spacing of ≈61.5 nm;[12] additional peaks corresponding to a hexagonal close packing (HCP) lattice were observed in simulated systems and in some experimental samples (Figure 2C, Figure S11).

The structure at $I = I_t$ consistently exhibited the highest order among the I values investigated for each VLP variant (Figure 2, Figures S10 and S12–S16). The ordered domain sizes of the arrays were estimated to be at least ≈400 nm in experiments regardless of the charge on the introduced peptides (Figure S16). While no significant assembly was found for $I > I_t$ (Figure 2B top left), assembled structures with a diminishing long-range order were observed when the ionic strength was lowered below I_t (Figure 2B, bottom left and right).

A collapse of the VLP-VLP PCFs for the 4 variants at their associated ionic strength threshold (I_t) was observed (Figure 2C). This indicates that while tuning the VLP charge changes I_t the structure of the array itself does not change. The vertical grid lines in Figure 2C indicate the peak positions of an FCC lattice (black) and an HCP lattice (dot-dashed orange); for $r < 3\sigma_v$, FCC peaks form a subset of those corresponding to HCP. The ordered array exhibited features corresponding to both FCC and HCP lattice structures. While experiments found the ordered arrays predominantly exhibit the FCC structure (Figure 2A), simulated array structures exhibited an order more consistent with HCP lattice. These differences could be attributed to the similar free energy of the FCC and HCP structures that the coarse-grained simulations were unable to resolve. Both FCC and HCP lattices have the same number of nearest neighbors and packing fraction ($\sqrt{2}\pi/6 \approx 0.74$); FCC has a slightly lower free energy (on the order of $0.001k_BT$ per particle for typical colloids).[36,37] It should be noted that while many samples exhibited the FCC lattice structure in experiments, some samples showed the presence of an HCP lattice structure[12] (Figure S11). Experiments with other VLPs and colloids have also found steady-state structures exhibiting a long-range order consistent with both FCC and HCP lattices.[38−42]

Condensed and Bridging Dendrimers. The number of dendrimers associated with the VLPs at the steady state were extracted from the simulation data to probe the mechanisms underlying the assembly of VLPs into ordered arrays and structures of a diminished long-range order. A condensed or bound dendrimer was defined as a dendrimer within 1.05 times the VLP−dendrimer contact distance (equal to the sum of the VLP and dendrimer radii). A bridging dendrimer was defined

DOI: 10.1021/acsabm.9b00166
ACS Appl. Bio Mater. 2019, 2, 2192−2201

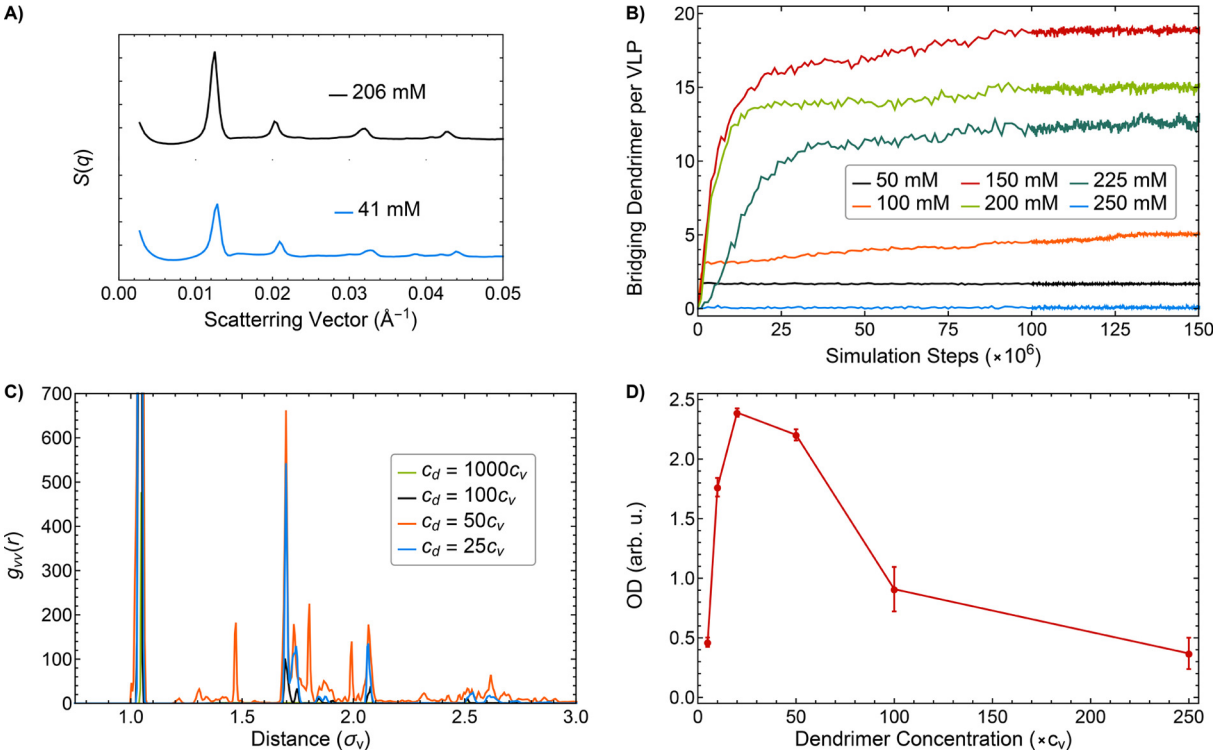

Figure 4. Studies of kinetic effects in the P22-E2 VLP assembly and structure. (A) SAXS structure factors showing that preformed ordered arrays assembled near the threshold I_t (with dendrimer concentration $c_d = 1000c_v$) persisted in an ordered state under low ionic strength conditions. (B) The average number of bridging dendrimers per P22-E2 VLP vs simulation steps (each step is equal to ≈4 ps). A distinctive lag phase is observed for the assembly of VLPs at I_t (dark green) that is absent for the bulk assembly at I away from the threshold. This trend generalizes to all charge variants. (C) VLP−VLP pair correlation functions $g_{vv}(r)$ for the P22-E2 system at a low ionic strength I = 10 mM and for a different c_d. Lowering c_d promotes the concurrency of dendrimer condensation and VLP aggregation time scales, restoring the bulk assembly at $c_d = 50c_v$ for a low I, where the original experiments with $c_d = 1000c_v$ did not show an appreciable assembly. (D) Optical density at λ = 800 nm as a function of c_d when P22-E2 is mixed with different amounts (c_d) of G6 dendrimers at I = 10 mM. Simulation-driven predictions are confirmed: the highest optical density is observed at $c_d \approx 50c_v$. Error bars indicate the standard deviation between three experimental replicates.

as a condensed dendrimer within this distance of two or more VLPs (i.e., a bridging dendrimer is a condensed dendrimer shared between multiple VLPs).

Figure 3A shows the average number of condensed dendrimers (N_c) on a VLP surface as a function of the ionic strength I for simulations associated with the aforementioned assembly studies of P22-E2, P22-Q2, P22-K2, and model mP22 variants. For all VLP variants, N_c increased as the ionic strength I was decreased in the vicinity of the threshold ionic strength I_t. N_c continued to rise as I was lowered further, saturating at very low values of I. A drop in N_c was observed for $I \ll I_t$ for some VLP variants. A similar number for $N_c \approx 24$ was found at I_t for each variant, regardless of the surface charge of the VLP. This number agreed with experiment[12] and indicated that about 24 G6 dendrimers are recruited by each P22 VLP variant to form the ordered arrays. FCC superlattices formed by Cowpea chlorotic mottle VLPs using gold nanoparticle linkers also exhibited the same number of linkers per VLP.[10]

The assembly was largely suppressed for low $I \lesssim 100 \ll 225$ mM, despite the significant condensation of dendrimers on the VLP surface ($N_c > 50$). The absence of spontaneous formation of VLP aggregates when $I \ll I_t$ could be attributed to the overcondensation of dendrimers and the associated increase in VLP−VLP repulsion. The ζ potential measurements found evidence for excessive condensation of dendrimers on the VLP surface: a positive ζ potential for P22-E2 was recorded for the $c_d = 1000c_v$ system at I = 10 mM (Figure S17).

Figure 3B shows the average number of bridging dendrimers, N_b, as a function of the scaled ionic strength, $I_s = I/I_t$. When I_s was decreased, N_b increased sharply to ≈12 at $I_s \approx 1$ ($I \approx I_t$) for all VLPs. This number agrees well with the number of nearest neighbors (12) in an FCC or HCP lattice and indicates there are two dendrimers between each bridged pair of VLPs. Further, the ratio of N_b to the number of condensed dendrimers, $\alpha = N_b/N_c$, was maximized at I_t (inset in Figure 3B). As I was lowered below I_t, α decreased while N_b continued to rise, albeit much more slowly. At a very low I, a sharp fall in N_b was observed, which correlated with the observation of the disappearance of large aggregates. The data for α as a function of I_s from different VLP variants showed a good collapse, suggesting a common mechanism across variants.

These results indicate that recruitment of dendrimers to bridge the VLPs while counteracting the VLP−VLP electrostatic repulsion and entropic forces is essential to the spontaneous bulk assembly of VLPs. Assembly is driven by the reduction in electrostatic energy as condensed dendrimers are bridged between VLPs. When each VLP maximizes the possibility of condensed dendrimers becoming bridging sites, it maximizes the number of its nearest neighbors, resulting in an ordered, close-packed array. The observed loss in the long-range order of the VLP aggregate as I was decreased indicates

DOI: 10.1021/acsabm.9b00166
ACS Appl. Bio Mater. 2019, 2, 2192−2201

that the attraction between dendrimer and VLP also needs to be sufficiently weak such that VLPs can sample the configuration space and avoid kinetic traps. For all VLP variants, at I_v, simulations found that the observed spontaneous formation of ordered arrays was characterized with a VLP−dendrimer binding energy of $\approx -5k_BT$ (here, binding energy indicates the minimum net VLP−dendrimer potential at the closest approach).

The connection between VLP−dendrimer attraction and the spontaneous formation of ordered arrays should be qualified with the role of the steric interactions in the VLP−dendrimer system, which are expected to play a critical role as indicated by previous experiments.[12] Simulations with VLPs exhibiting stronger steric repulsion compared to P22-E2 showed that such VLPs form ordered arrays but at a lower ionic strength than the I_t associated with P22-E2 system (Figure S18). In the coarse-grained model, the steric interaction between dendrimers and VLPs is tuned by the σ_{hc} parameter; eq 2. σ_{hc} effectively accounts for the dendrimer proximity to the VLP surface; σ_{hc} = 6.7 nm for P22-E2. VLPs with σ_{hc} = 6.3 nm, which increases the effective VLP−dendrimer steric repulsion, did not exhibit any assembly at I = 225 mM (the ionic strength threshold at which simulations observed the assembly of P22-E2 VLPs into an ordered array). However, upon further lowering of the ionic strength to 200 mM, the optimal balance between electrostatic and steric interactions was restored, and ordered arrays similar to the original P22-E2 simulations were observed (Figure S18). Steric effects are difficult to quantify in experiments, so the simulation-driven assertion of changes in ionic strength threshold for assembly arising from variations in steric features of the VLPs is not yet validated, but informs future experiments.

Kinetic Effects and Role of Dendrimer Concentration. The aforementioned studies showed that, when starting from a mixed state, VLPs assembled but with a diminishing order for ionic strengths below the threshold ($I < I_t$). The origin of disorder at a low I was probed further using the P22-E2 VLP system. Starting with an ordered array formed at $I \approx I_t$ and dialyzing out the salt in experiments showed that the ordered structure persisted at lower ionic strengths (Figure 4A, Figure S19). The same result was observed in simulations, which confirmed that the preassembled ordered array persisted even upon significant increase in the number of condensed dendrimers at a low I (Figure S20). These results indicate that, for $I < I_t$ the electrostatics-driven assembly of VLPs into ordered clusters is still thermodynamically favorable.

The inability of the mixture of VLPs and dendrimers to achieve the thermodynamically favored ordered array structure for ionic strengths lower than I_t suggests the possibility that VLPs are kinetically trapped in an amorphous aggregate. For these I values, the attraction between dendrimer and VLP dominates the dynamics, leading to rapid condensation and subsequent bridging of VLPs. The formation of bridging sites $N_b(t)$ as a function of time t was tracked in simulations, and the results are shown in Figure 4B. For $I \approx I_v$, the rise in $N_b(t)$ exhibited a lag phase before saturation with a time scale ($\approx$20 million simulation steps) comparable to the time scale of the aggregation of VLPs into arrays ($\approx$100 million steps). For ionic strengths smaller but closer to I_t (125 mM < I < 200 mM), a relatively sharper rise in $N_b(t)$ was observed, shrinking the time scale of the lag phase by an order of magnitude ($\approx$1 million steps). The reduced time scale of the lag phase leads to a nonoptimal bridging of VLPs by dendrimers such that the VLPs become locked into place and are unable to reorganize into the thermodynamically favored structure. The diminished lag phase associated with the formation of amorphous aggregates resembles effects seen in individual virus capsid formation where capsomeres rapidly self-assemble into thermodynamically less-favored intermediate states, producing a kinetic bottleneck that prevents assembly into complete capsids.[43,44]

Figure 4B shows that, for $I \lesssim 100$ mM $\ll I_v$, the time scale for the formation of bridging sites is prohibitively large to enable cluster formation. Simulations showed that the number of condensed dendrimers rose rapidly under these conditions (approaching values of $\approx$90−120; Figure S20). While simulations overestimate the extent of condensation of dendrimers on the VLP surface at these low I values, experiments show that the dendrimer condensation is still significant enough to induce a net VLP charge reversal (Figure S17). Figure 4B shows that this charge reversal is on a much shorter time scale than the time scale associated with the aggregation of VLPs, preventing assembly into larger clusters.

These observations suggest that for the spontaneous formation of ordered arrays, dendrimer−VLP attraction must be strong enough to induce sufficient condensation of dendrimers for bridge-driven VLP aggregation. On the other hand, this attraction must also be sufficiently weak to prevent rapid overcondensation and to enable subsequent VLP rearrangements within experimentally accessible time scales. Starting with an already assembled array of VLPs and lowering I (Figure 4A) is equivalent to assuming that the time scale for VLP aggregate formation is extremely short such that it is comparable to the time scale for dendrimer condensation and formation of bridging sites. Thus, the array configuration persisted despite significant dendrimer condensation on the VLPs under these conditions (approaching values of $\approx$100, nearly the same as is seen to inhibit assembly from a mixed state; Figure S20).

These results indicate that modulating the dendrimer concentration c_d can control the potential of overcondensation of dendrimers on the VLP surface (Figure S17), such that VLPs can exhibit a significant bulk assembly for $I \ll I_t$. Lowering c_d reduces the dendrimer condensation rate and slows down the rise in formation of bridging sites with time (Figure S21), stretching the lag phase and enabling the VLPs to reorganize into aggregates. At I = 10 mM, simulations of the P22-E2 system showed that $c_d = 25c_v$, $50c_v$ cases could yield a significantly greater bulk assembly than the $c_d = 1000c_v$, $100c_v$ systems (Figure 4C). The optical density data from new experiments and dynamic light scattering measurements under the same conditions confirmed these predictions (Figure 4D and Figure S22).

MODEL LIMITATIONS

Some quantitative differences between simulation results and experimental data were observed, highlighting limitations of the coarse-grained model. As noted before, a larger VLP aggregate size was recorded in experiments compared to simulations at ionic strengths much lower than the threshold. Further, under the same ionic conditions, a smaller number of condensed dendrimers (by roughly a factor of 2) were recorded in experiments[12] compared to simulations.

These disagreements can be attributed to effects neglected in the coarse-grained model such as the condensation of counterions on VLP and dendrimer surfaces and ion−ion

DOI: 10.1021/acsabm.9b00166
ACS Appl. Bio Mater. 2019, 2, 2192−2201

correlations, which are expected to alter the effective charges of VLPs and dendrimers at a lower I. The number of condensed dendrimers on the VLP surface is also expected to be limited because the VLP surface is not homogeneously charged as assumed in simulations. Patches of a positive charge on the VLP surface will repel the dendrimers; while negatively charged regions of the surface will attract more dendrimers, the associated dendrimer−dendrimer electrostatic repulsion is expected to result in a net reduction in the number of condensed dendrimers compared to the homogeneously (negatively) charged model of the VLP surface. Further, simulations neglect the deformable[45] and dendritic structure of dendrimers that could result in full saturation of the VLP surface by a relatively fewer number of condensed dendrimers. All of these effects could inhibit extensive overcondensation of dendrimers on the VLPs under low ionic strengths, resulting in a greater capacity to assemble into aggregates of larger sizes than is observed in simulations.

Additionally, unlike simulated models, experimental systems are subjected to local and temporal inhomogeneities, which may influence the bulk assembly. For example, in the case of systems with $c_d = 1000c_v$, the initial dendrimer concentration may be lower than $1000c_v$ over localized regions in the experimental samples to suppress overcondensation of dendrimers and induce the bulk assembly at the lower ionic strength values. The ability to measure kinetics of the bulk assembly in experiments may provide useful information to correlate with simulation data for $N_b(t)$ and help further refine the coarse-grained model. Finally, finite-size effects in simulations limit the extent of ordered array sizes observed as well as the associated number of peaks in the PCFs. Resolving these issues by simulating larger systems could enable a more accurate characterization of array structures from simulation data.

CONCLUSIONS

Using integrated experimental characterization methods and molecular dynamics simulations of a coarse-grained model, we showed that the spontaneous assembly of VLPs into three-dimensional, ordered arrays can be controlled and tuned by changing the VLP surface charge. The threshold ionic strength I_t for VLP array formation decreased with the VLP surface charge. For ionic strengths below I_t, spontaneous assembly continued to occur but yielded structures with a reduced long-range order.

Results demonstrate that the self-assembly of VLPs into ordered arrays is driven by the balance between the dendrimer−VLP attraction and the VLP thermal motion. The reduction in electrostatic energy resulting from the condensed dendrimers bridging between VLPs counteracts the VLP electrostatic repulsion and their thermal motion. The optimal dendrimer−VLP attraction facilitates the formation of dendrimer bridging sites at a time scale comparable to the VLP rearrangements such that the VLPs are able to avoid kinetic traps in favor of adopting an ordered array structure.

A systematic analysis of the kinetic effects driven by simulations showed that the capacity to form arrays can be further enhanced by modulating the dendrimer concentration c_d and predicted that lowering the c_d could result in a larger bulk VLP aggregation at low ionic strengths where previous experiments only found diminished assembly.[12] These predictions were tested and validated by new experiments where a significant optical density was observed in VLP−dendrimer solutions with a lower c_d for ionic strengths much lower than the threshold value. Such simulation-driven predictions open new pathways for controlling the assembly of VLPs and can drive future experiments.

Recent experiments have investigated the use of dendrimer features including size and charge to engineer an ordered assembly of VLPs.[31,46] The integrated approach presented here complements these experimental findings and expands the strategies to control and manipulate a higher-order assembly using other VLPs and linkers.[10] The method can be extended to investigate mixtures of multiple VLP variants as well as mixtures of dendrimers of different generations; such studies are in progress. Investigating different VLP-linker systems may require an adjustment of the parameters associated with the steric interactions to appropriately account for the variation in important linker features such as linker flexibility and surface inhomogeneities; some linkers (e.g., lower generation PAMAM dendrimers such as G3) will likely require a finer-grained model description. Larger system sizes will become necessary to finely resolve the nature of the ordered VLP array structure via the computation of the pair correlation functions. Complementary advances in the experiment to accurately assess the number of condensed and bridging linkers may further improve our ability to configure systems that form robust, large-scale superlattices based on VLP-linker building blocks.

ASSOCIATED CONTENT

Supporting Information

The Supporting Information is available free of charge on the ACS Publications website at DOI: 10.1021/acsabm.9b00166.

Details of the model, simulation, experimental methods, simulation snapshots, pair correlation functions, bridging dendrimer statistics, experimental measurements of VLP features, structure factors from SAXS data, and DLS measurement data (PDF)

AUTHOR INFORMATION

Corresponding Authors

*E-mail: nbrunk@iu.edu.
*E-mail: muchida@indiana.edu.
*E-mail: blee@anl.gov.
*E-mail: fukuto@bnl.gov.
*E-mail: lyang@bnl.gov.
*E-mail: trevdoug@iu.edu.
*E-mail: vjadhao@iu.edu.

ORCID

Nicholas E. Brunk: 0000-0001-5444-799X
Masaki Uchida: 0000-0003-0710-8834
Byeongdu Lee: 0000-0003-2514-8805
Trevor Douglas: 0000-0002-7882-2704
Vikram Jadhao: 0000-0002-8034-2654

Author Contributions

⊥N.E.B. and M.U. contributed equally to this work.

Notes

The authors declare no competing financial interest.

ACKNOWLEDGMENTS

Computational modeling and simulations in this work were supported by the National Science Foundation through grant nos. 1720625 and DMR-1753182, as well as by Indiana

DOI: 10.1021/acsabm.9b00166
ACS Appl. Bio Mater. 2019, 2, 2192−2201

University (IU) through startup funds. Simulations were performed using the Big Red II supercomputing system supported in part by Lilly Endowment, Inc., through its support for the IU Pervasive Technology Institute, and in part by the Indiana METACyt Initiative. The IU Data Capacitor storage space is supported by the National Science Foundation under grant no. CNS-0521433. Experimental studies and characterization of VLP arrays were supported by the U.S. Department of Energy (DOE), Office of Basic Energy Sciences, Division of Materials Sciences and Engineering (DE-SC0016155). The BNL contribution to this work was supported by the U.S. Department of Energy, Basic Energy Sciences, by the Materials Sciences and Engineering Division (M.F.), and by the National Synchrotron Light Source II (M.F. and L.Y.), under contract no. DE-AC02-98CH10886. L.Y. is also supported by DOE-BER under contract no. DE-KP1605010 and by NIH-NIGMS under grant no. P41GM111244. This research used Beamline X9 of the National Synchrotron Light Source, a U.S. Department of Energy (DOE), Office of Science User Facility operated for the DOE Office of Science by Brookhaven National Laboratory under contract no. DE-AC02-98CH10886 with additional support from NIH through grant no. S10 OD012331. This research also used resources of the Advanced Photon Source, a U.S. Department of Energy (DOE), Office of Science User Facility operated for the DOE Office of Science by Argonne National Laboratory under contract no. DE-AC02-06CH11357. We thank the Nanoscale Characterization Facility, the Mass Spectrometry Facility, and Electron Microscopy Center at IU Bloomington for access to their instrumentation.

REFERENCES

(1) Whitesides, G. M.; Grzybowski, B. Self-assembly at all scales. *Science* **2002**, *295*, 2418−2421.
(2) Glotzer, S.; Solomon, M.; Kotov, N. A. Self-assembly: From nanoscale to microscale colloids. *AIChE J.* **2004**, *50*, 2978−2985.
(3) Aizenberg, J. Crystallization in Patterns: A Bio-Inspired Approach. *Adv. Mater.* **2004**, *16*, 1295−1302.
(4) Bishop, K. J.; Wilmer, C. E.; Soh, S.; Grzybowski, B. A. Nanoscale forces and their uses in self-assembly. *Small* **2009**, *5*, 1600−1630.
(5) Cigler, P.; Lytton-Jean, A. K.; Anderson, D. G.; Finn, M.; Park, S. Y. DNA-controlled assembly of a NaTl lattice structure from gold nanoparticles and protein nanoparticles. *Nat. Mater.* **2010**, *9*, 918.
(6) Macfarlane, R. J.; Lee, B.; Jones, M. R.; Harris, N.; Schatz, G. C.; Mirkin, C. A. Nanoparticle superlattice engineering with DNA. *Science* **2011**, *334*, 204−208.
(7) Li, F.; Josephson, D. P.; Stein, A. Colloidal assembly: the road from particles to colloidal molecules and crystals. *Angew. Chem., Int. Ed.* **2011**, *50*, 360−388.
(8) Kostiainen, M. A.; Kasyutich, O.; Cornelissen, J. J.; Nolte, R. J. Self-assembly and optically triggered disassembly of hierarchical dendron−virus complexes. *Nat. Chem.* **2010**, *2*, 394.
(9) Zhang, Y.; Lu, F.; Yager, K. G.; Van Der Lelie, D.; Gang, O. A general strategy for the DNA-mediated self-assembly of functional nanoparticles into heterogeneous systems. *Nat. Nanotechnol.* **2013**, *8*, 865.
(10) Kostiainen, M. A.; Hiekkataipale, P.; Laiho, A.; Lemieux, V.; Seitsonen, J.; Ruokolainen, J.; Ceci, P. Electrostatic assembly of binary nanoparticle superlattices using protein cages. *Nat. Nanotechnol.* **2013**, *8*, 52.
(11) Uchida, M.; LaFrance, B.; Broomell, C. C.; Prevelige, P. E., Jr; Douglas, T. Higher Order Assembly of Virus-like Particles (VLPs) Mediated by Multi-valent Protein Linkers. *Small* **2015**, *11*, 1562−1570.
(12) Uchida, M.; McCoy, K.; Fukuto, M.; Yang, L.; Yoshimura, H.; Miettinen, H. M.; LaFrance, B.; Patterson, D. P.; Schwarz, B.; Karty, J. A.; Prevelige, P. E.; Lee, B.; Douglas, T. Modular Self-Assembly of Protein Cage Lattices for Multistep Catalysis. *ACS Nano* **2018**, *12*, 942−953.
(13) Mirkin, C. A. The Polyvalent Gold Nanoparticle Conjugate-Materials Synthesis, Biodiagnostics, and Intracellular Gene Regulation. *MRS Bull.* **2010**, *35*, 532−539.
(14) Jones, M. R.; Seeman, N. C.; Mirkin, C. A. Programmable materials and the nature of the DNA bond. *Science* **2015**, *347*, 1260901.
(15) Fan, J. A.; He, Y.; Bao, K.; Wu, C.; Bao, J.; Schade, N. B.; Manoharan, V. N.; Shvets, G.; Nordlander, P.; Liu, D. R.; Capasso, F. DNA-Enabled Self-Assembly of Plasmonic Nanoclusters. *Nano Lett.* **2011**, *11*, 4859−4864.
(16) Zhang, R.; Jha, P. K.; De La Cruz, M. O. Non-equilibrium ionic assemblies of oppositely charged nanoparticles. *Soft Matter* **2013**, *9*, 5042−5051.
(17) Aumiller, W. M.; Uchida, M.; Douglas, T. Protein cage assembly across multiple length scales. *Chem. Soc. Rev.* **2018**, *47*, 3433−3469.
(18) McCoy, K.; Uchida, M.; Lee, B.; Douglas, T. Templated Assembly of a Functional Ordered Protein Macromolecular Framework from P22 Virus-like Particles. *ACS Nano* **2018**, *12*, 3541−3550.
(19) Prodan, E.; Radloff, C.; Halas, N. J.; Nordlander, P. A hybridization model for the plasmon response of complex nanostructures. *Science* **2003**, *302*, 419−422.
(20) Sun, J.; DuFort, C.; Daniel, M.-C.; Murali, A.; Chen, C.; Gopinath, K.; Stein, B.; De, M.; Rotello, V. M.; Holzenburg, A.; Kao, C. C.; Dragnea, B. Core-controlled polymorphism in virus-like particles. *Proc. Natl. Acad. Sci. U. S. A.* **2007**, *104*, 1354−1359.
(21) Asor, R.; Ben-nun Shaul, O.; Oppenheim, A.; Raviv, U. Crystallization, reentrant melting, and resolubilization of virus nanoparticles. *ACS Nano* **2017**, *11*, 9814−9824.
(22) Kostiainen, M. A.; Hiekkataipale, P.; de la Torre, J. Á.; Nolte, R. J.; Cornelissen, J. J. Electrostatic self-assembly of virus−polymer complexes. *J. Mater. Chem.* **2011**, *21*, 2112−2117.
(23) Marson, R. L.; Nguyen, T. D.; Glotzer, S. C. Rational design of nanomaterials from assembly and reconfigurability of polymer-tethered nanoparticles. *MRS Commun.* **2015**, *5*, 397−406.
(24) Li, T. I.; Sknepnek, R.; Macfarlane, R. J.; Mirkin, C. A.; Olvera de la Cruz, M. Modeling the Crystallization of Spherical Nucleic Acid Nanoparticle Conjugates with Molecular Dynamics Simulations. *Nano Lett.* **2012**, *12*, 2509−2514.
(25) Orlik, R.; Mitus, A.; Kowalczyk, B.; Patashinski, A.; Grzybowski, B. Computer simulation of self-assembly (crystallization) of oppositely charged nanoparticles with various size distributions. *J. Non-Cryst. Solids* **2009**, *355*, 1360−1369.
(26) Hagan, M. F.; Zandi, R. Recent advances in coarse-grained modeling of virus assembly. *Curr. Opin. Virol.* **2016**, *18*, 36.
(27) Kowalczyk, B.; Kalsin, A. M.; Orlik, R.; Bishop, K. J.; Patashinskii, A. Z.; Mitus, A.; Grzybowski, B. A. Size selection during crystallization of oppositely charged nanoparticles. *Chem. - Eur. J.* **2009**, *15*, 2032−2035.
(28) Leunissen, M. E.; Christova, C. G.; Hynninen, A.-P.; Royall, C. P.; Campbell, A. I.; Imhof, A.; Dijkstra, M.; Van Roij, R.; Van Blaaderen, A. Ionic colloidal crystals of oppositely charged particles. *Nature* **2005**, *437*, 235.
(29) Hynninen, A.-P.; Christova, C. G.; van Roij, R.; van Blaaderen, A.; Dijkstra, M. Prediction and Observation of Crystal Structures of Oppositely Charged Colloids. *Phys. Rev. Lett.* **2006**, *96*, 138308.
(30) Royall, C.; Leunissen, M.; Van Blaaderen, A. A new colloidal model system to study long-range interactions quantitatively in real space. *J. Phys.: Condens. Matter* **2003**, *15*, S3581.
(31) Palchoudhury, S.; Zhou, Z.; Ramasamy, K.; Okirie, F.; Prevelige, P. E.; Gupta, A. Self-assembly of P22 protein cages with polyamidoamine dendrimer and inorganic nanoparticles. *J. Mater. Res.* **2017**, *32*, 465−472.

DOI: 10.1021/acsabm.9b00166
ACS Appl. Bio Mater. 2019, 2, 2192−2201

(32) Boon, N.; Guerrero-García, G. I.; van Roij, R.; Olvera de la Cruz, M. Effective charges and virial pressure of concentrated macroion solutions. *Proc. Natl. Acad. Sci. U. S. A.* **2015**, *112*, 9242−9246.
(33) Hunter, R. J. *Zeta potential in colloid science: principles and applications*; Academic press, 2013; Vol. 2.
(34) Božič, A. L.; Šiber, A.; Podgornik, R. How simple can a model of an empty viral capsid be? Charge distributions in viral capsids. *J. Biol. Phys.* **2012**, *38*, 657−671.
(35) Pericet-Camara, R.; Papastavrou, G.; Borkovec, M. Effective charge of adsorbed poly (amidoamine) dendrimers from direct force measurements. *Macromolecules* **2009**, *42*, 1749−1758.
(36) Mahynski, N. A.; Panagiotopoulos, A. Z.; Meng, D.; Kumar, S. K. Stabilizing colloidal crystals by leveraging void distributions. *Nat. Commun.* **2014**, *5*, 4472.
(37) Woodcock, L. Entropy difference between the face-centred cubic and hexagonal close-packed crystal structures. *Nature* **1997**, *385*, 141.
(38) Pusey, P.; Van Megen, W.; Bartlett, P.; Ackerson, B.; Rarity, J.; Underwood, S. Structure of crystals of hard colloidal spheres. *Phys. Rev. Lett.* **1989**, *63*, 2753.
(39) Gasser, U.; Weeks, E. R.; Schofield, A.; Pusey, P.; Weitz, D. Real-space imaging of nucleation and growth in colloidal crystallization. *Science* **2001**, *292*, 258−262.
(40) Auer, S.; Frenkel, D. Numerical prediction of absolute crystallization rates in hard-sphere colloids. *J. Chem. Phys.* **2004**, *120*, 3015−3029.
(41) Pronk, S.; Frenkel, D. Can stacking faults in hard-sphere crystals anneal out spontaneously? *J. Chem. Phys.* **1999**, *110*, 4589−4592.
(42) Zhu, J.; Li, M.; Rogers, R.; Meyer, W.; Ottewill, R.; Russel, W.; Chaikin, P. Crystallization of hard-sphere colloids in microgravity. *Nature* **1997**, *387*, 883.
(43) Zandi, R.; van der Schoot, P.; Reguera, D.; Kegel, W.; Reiss, H. Classical nucleation theory of virus capsids. *Biophys. J.* **2006**, *90*, 1939−1948.
(44) Hagan, M. F.; Elrad, O. M. Understanding the concentration dependence of viral capsid assembly kineticsthe origin of the lag time and identifying the critical nucleus size. *Biophys. J.* **2010**, *98*, 1065−1074.
(45) Li, J.; Piehler, L.; Qin, D.; Baker, J.; Tomalia, D.; Meier, D. Visualization and characterization of poly (amidoamine) dendrimers by atomic force microscopy. *Langmuir* **2000**, *16*, 5613−5616.
(46) Liljestrom, V.; Seitsonen, J.; Kostiainen, M. A. Electrostatic self-assembly of soft matter nanoparticle cocrystals with tunable lattice parameters. *ACS Nano* **2015**, *9*, 11278−11285.

DOI: 10.1021/acsabm.9b00166
ACS Appl. Bio Mater. 2019, 2, 2192−2201

Supporting Information for "Linker-mediated Assembly of Virus-like Particles into Ordered Arrays via Electrostatic Control"

Nicholas E. Brunk,[*,†,⊥] Masaki Uchida,[*,‡,⊥] Byeongdu Lee,[*,¶] Masafumi Fukuto,[*,§,‖] Lin Yang,[*,§] Trevor Douglas,[*,‡] and Vikram Jadhao[*,†]

†*Intelligent Systems Engineering, Indiana University, Bloomington, Indiana 47408*

‡*Department of Chemistry, Indiana University, Bloomington, Indiana 47408*

¶*X-Ray Science Division, Advanced Photon Source, Argonne National Laboratory, 9700 South Cass Avenue, Illinois 60439*

§*National Synchrotron Light Source II, Brookhaven National Laboratory, Upton, New York 11973*

‖*Condensed Matter Physics and Materials Science Department, Brookhaven National Laboratory, Upton, New York 11973*

⊥*Contributed equally to this work*

E-mail: nbrunk@iu.edu; muchida@indiana.edu; blee@aps.anl.gov; fukuto@bnl.gov; lyang@bnl.gov; trevdoug@iu.edu; vjadhao@iu.edu

Experimental Details

Modulating surface charge of P22 VLPs by genetic engineering: Three variants of the P22 VLPs possessing different surface charges were prepared by genetic engineering of the C-terminus of the P22 Coat Protein (CP). Two repeats of either a net negatively charged peptide with sequence VAALEKE (E2 peptide), a neutral peptide with sequence VAALQSQ (Q2 peptide), or

net positively charged peptide with sequence VAALKEK (K2 peptide) were introduced at the C-terminus of the CP, which is exposed to the exterior of the VLP (hereafter referred to as CP-E2, CP-Q2 and CP-K2).[1] Because the P22 VLP is assembled from 420 copies of CP, up to 420 copies of the E2, Q2 or K2 peptides are displayed on the outside of the P22 VLP for each mutant. The P22 VLP variants with the E2 peptide, Q2 peptide and the K2 peptide are referred to as P22-E2, P22-Q2 and P22-K2, respectively. The DNA and amino acids sequences of CP-E2, CP-N2 and CP-K2 are shown below, after the primary SI text.

Expression and purification of P22-E2, P22-Q2, P22-K2 VLPs: The three variants of P22 VLPs were expressed and purified using an established procedure described elsewhere.[2,3] Briefly, a truncated P22 scaffolding protein (SP141) and an engineered CP were cloned into the first and the second cloning sites of the pRSFDuet-1 vector (Novagen), respectively. The vector was transformed into BL21 (DE3) E. coli strain (New England Biolabs) for protein expression. E. coli containing each vector was cultured in LB medium at 37°C in the presence of 30 μg/mL kanamycin to maintain selection pressure. Expression of the SP141 and a CP mutant was induced by isopropyl -D-thiogalactopyranoside (IPTG) to a final concentration of 0.3 mM when the OD at 600 nm of the culture medium reached 0.6 a.u. The cells were allowed to grow for an additional 4h, then harvested and stored at -80°C until the P22 VLPs were purified. The P22 VLPs self-assembled from SP141 and CP *in vivo* were purified via ultracentrifugation at 45,000 rpm over a 35% (w/v) sucrose cushion followed by size exclusion chromatography with a Sephacryl S-500 HR column (GE Healthcare Life Sciences). P22 VLPs were pelleted by ultracentrifugation and then re-suspended in phosphate buffers with various ionic strengths.

Characterization of P22 VLPs: Molecular weights of CP mutants with three different peptides were measured with ESI-Q-TOF mass spectrometry (Synapt G2S, Waters, Milford, MA) interfaced to an Acquity ultra performance liquid chromatography (UPLC; Waters) equipped with a reverse phase column (Jupiter C4 5 μm 300 Å, Phenomenex) (Fig. S2). Two microliters of the P22 sample (0.8 mg/mL) were loaded onto the column and then eluted through a gradient of

100% 0.1% formic acid in H_2O to 100% 0.1% formic acid in Acetonitrile. The deconvoluted average mass of a protein was obtained from a multiple charge state distribution and compared with a calculated molecular weight for each mutant. The overall cage-like morphology (Fig. S1) and hydrodynamic diameter (Fig. S3) of P22 VLP mutants were analyzed with transmission electron microscopy (TEM; JEM 1010 transmission electron microscope, JEOL Ltd., Akishima, Japan) and dynamic light scattering (DLS; Zetasizer Nano ZS, Malvern Instruments, Worcestershire, UK)3.

Zeta-potentials of each P22 mutant in buffer solution (sodium phosphate 10 mM, sodium chloride 20 mM, pH 7.0) were measured using Zetasizer Nano ZS (Malvern Instruments) (Fig. S4A). The Smoluchowski approximation was used to convert the electrophoretic mobility to zeta-potential. The surface charge of P22 VLPs was also qualitatively assessed using a native agarose gel. A horizontal 1% agarose gel was prepared using a Tris-acetate (TAE) buffer (Tris-base 40 mM, sodium acetate 20 mM EDTA 1 mM, pH 8.2) (Fig. S4B). The P22 VLP samples were mixed with sample buffer (25 mM sodium phosphate, 1 mM magnesium chloride, 20% sucrose, 0.02% bromophenyl blue, pH 7.4) at 1:1 (vol/vol) ratio prior to loading. The samples were subjected to electrophoresis in the TAE buffer for 3 hours at a constant voltage of 65 V. The proteins were detected after staining with Coomassie brilliant blue R-250.

Dendrimer-mediated assembly of P22 VLPs into three-dimensional arrays: Positively charged generation 6 polyamidoamine dendrimer (PAMAM G6; Sigma Aldrich, St. Louis, MO) has been shown to mediate higher order assembly of negatively VLPs.[3–5] In this study, three types of P22 VLP variants with different surface charges were mixed with PAMAM G6 under various ionic strengths. The VLP concentration in all experiments was held constant at $c_v = 37$ nM or a packing fraction of $\phi_v \approx 0.002$. The packing fraction ϕ_v was calculated as the ratio of the volume of the VLPs to the volume of the solution: $\phi_v = c_v V_v$, where c_v is the virus concentration (in nm^{-3}) and V_v is the volume of an individual virus (in nm^3). The dendrimer-mediated array formation of VLPs was first assessed by the increase in turbidity upon mixing the solutions (Fig. 1). Typically, 150 microliters of P22 VLP solution (50 nM VLP) in a phosphate buffer solution

was mixed with PAMAM G6 at a defined denderimer-VLP ratio (typically, 1000 dendrimers per VLP). The dendrimer solution was diluted with the same buffer solution at a ratio of 1:4 (vol/vol) beforehand. The increase in optical density of the VLP solutions was measured 30 min after mixing with the dendrimer solution on a UV-Vis spectrometer (Agilent 8453) at 800 nm and at room temperature. Because neither individual P22 VLPs nor dendrimer exhibit absorbance at 800 nm, observed optical density is attributed to scattering due to the formation of large particles. Four individual samples were measured at each data point yielding the average values and standard deviation. The size of the higher order assembly of VLPs in the solutions was analyzed using DLS (Fig. S6 and Fig. S22). Zeta potentials of VLP assemblies with various amount of G6 dendrimer at I = 5 mM (sodium phosphate 2.5 mM, sodium chloride 5 mM, pH 7.0) was determined by electrophoretic mobility measurements on a Malvern Zetasizer Nano ZS (Fig. S17).

Measurement of ionic strength threshold values: The ionic strength threshold indicating the onset of assembly for each VLP variant was estimated based on the change in the turbidity of the VLP solution when mixed with dendrimer solution at different ionic strengths (Fig. 1A of the main paper). Four individual samples of the same variant were measured at each I. Within the range of I values examined, there was a significant difference in the turbidity (optical density) for all P22 variants between the solution of the highest I at which P22 variant still assembled into arrays and that of the next higher ionic strength data point. For example, higher-order assembly of P22-E2 was initially examined at $I = 206, 247$, and 288 mM (besides other lower and higher ionic strengths). All four sample solutions at $I = 206$ and 247 mM showed drastic increase in optical density while solutions at $I = 288$ mM showed no significant increase. To refine the assay, higher order assembly at $I = 267$ mM was investigated as an addition, and all samples showed almost zero change in optical density. Based on this set of observations, the ionic strength threshold of P22-E2 was defined as $I_t = 247$ mM, which can be considered accurate up to the ionic strength increment of ≈ 20 mM. Estimates of uncertainty in the threshold values can be made more precise by examining the turbidity at finer ionic strength increments (e.g., measuring at multiple I values

between 247 and 267 mM for P22-E2).

The use of freshly defrosted samples (i.e., little peptide cleavage) in the current set of experiments yielded consistent results with very little effect of sample variability on the threshold values. We note that earlier studies have shown some variation in ionic threshold due to sample variability (likely due to cleavage of surface-exposed peptides over time); for example, threshold values as low as $I_t = 206$ mM have been recorded for P22-E2.[3]

Structure analysis of VLP arrays with Small-angle X-ray scattering (SAXS): The structure of the VLP arrays was interrogated with small-angle x-ray scattering (SAXS) at the X9 beamline at the National Synchrotron Light Source (NSLS) and the 12ID-B beamline at the Advanced Photon Source (APS). All the samples were subjected to the SAXS measurements in the buffer solutions as prepared. The measurements were carried out at 13.5 keV (X9) or at 14 keV (12ID-B) and the two-dimensional scattering data were collected with a Pilatus 1M detector at the X9 and a Pilatus 2M detector at the 12ID-B. Scattering angle was calibrated using silver behenate as a standard. One-dimensional SAXS profiles were acquired via averaging the two-dimensional scattering patterns. The data were represented as scattering intensity as a function of (the modulus of) scattering vector q:

$$q = \frac{4\pi}{\lambda} \sin(\theta) \tag{1}$$

where θ is half of the scattering angle and λ is the x-ray wavelength used for the measurements. Dark current frames and scattering of buffers were measured and subtracted from all data.

The overall x-ray scattering intensity $I(q)$, which is experimentally acquired by the SAXS measurement of the P22 array samples, consist of two contributions to the x-ray scattering: the form factor $P(q)$, which is inherent to the sizes and shapes of individual nanoparticles, and the structure factor $S(q)$, which is inherent to the arrangement of these nanoparticles relative to one another. The $P(q)$ of each P22 VLP mutant was obtained by measuring the SAXS profile of monodisperse P22 VLPs in a buffer solution. The $S(q)$ of the array samples was extracted from the measured $I(q)$ as described in the previous paper by using the $P(q)$.[3] Briefly, $I(q)$ is the

following combination[6] of $P(q)$ and $S(q)$:

$$I(q) = kP(q)S(q) \tag{2}$$

The constant k is a factor related to the concentration of particles. The experimentally measured small-angle x-ray scattering profile $I(q)$ of each sample is presented in Fig. S12. The comparison between measured $I(q)$, modeled $kP(q)$, and extracted $S(q)$ are presented in Fig. S13 to Fig. S19.

Estimating crystalline domain size from SAXS: Width of the x-ray diffraction peaks is a convenient parameter to assess crystallinity of samples because crystalline domain size is inversely proportional to the x-ray diffraction peak width.[6] In this study, crystalline domain size was estimated using the full width at half maximum (FWHM) of the first order diffraction peaks of each sample and the Scherrer equation as described previously[3] (Fig. S16). The first order diffraction peak was fit with Gaussian functions to determine the FWHM. Instrumental resolution Δq_{inst}, which leads to peak broadening, was taken into account and the resolution-corrected FWHM of a sample peak, Δq_{samp}, is given by the following form for a convolution of two Gaussians:

$$\Delta q_{samp} = \sqrt{\Delta q_{obs}^2 - \Delta q_{inst}^2}, \tag{3}$$

where Δq_{obs} is the FWHM of an observed diffraction peak, and Δq_{inst} for our measurement is approximately 0.0005 $\mathrm{\AA}^{-1}$. Crystalline domain size d was estimated using the Scherrer equation:

$$d = \frac{K\lambda}{\beta \cos(\theta)} \tag{4}$$

where K is Scherrer's constant, λ is the x-ray wavelength used for the measurements (0.8856 $\mathrm{\AA}$), β is the resolution-corrected peak width in radians, and θ is half of the scattering angle. Although the value of K depends on factors such as geometry of the crystallites, 0.9 may be taken for roughly equant crystallites when the FWHM is used as the measure of peak width.[7,8]

DNA sequences of proteins used in this study:

CP with E2 (CP-E2)

ATG GCT TTG AAC GAA GGT CAA ATT GTT ACA CTG GCG GTA GAT GAA ATC ATC GAA ACC ATC TCC GCA ATC ACT CCA ATG GCG CAG AAA GCC AAG AAA TAC ACC CCG CCT GCT GCT TCT ATG CAG CGC TCC AGC AAT ACC ATC TGG ATG CCT GTA GAG CAA GAG TCA CCC ACT CAG GAG GGC TGG GAT TTA ACT GAT AAA GCG ACA GGG TTA CTG GAA CTT AAC GTC GCG GTA AAC ATG GGA GAG CCG GAT AAC GAC TTC TTC CAG TTG CGT GCT GAT GAC TTG CGA GAC GAA ACT GCG TAT CGT CGC CGC ATC CAG TCT GCC GCT CGC AAG CTG GCG AAC AAC GTT GAG TTG AAA GTC GCA AAC ATG GCC GCC GAG ATG GGT TCG CTG GTT ATC ACC TCC CCT GAT GCC ATC GGC ACT AAT ACC GCA GAC GCC TGG AAC TTT GTG GCC GAC GCA GAA GAA ATC ATG TTC TCC CGC GAA CTT AAC CGC GAC ATG GGG ACA TCG TAC TTC TTC AAC CCT CAG GAC TAC AAA AAA GCG GGT TAC GAC CTG ACC AAG CGT GAC ATC TTC GGG CGT ATT CCT GAA GAA GCA TAC CGA GAT GGC ACC ATT CAG CGT CAG GTC GCT GGC TTC GAT GAT GTC CTG CGC TCT CCG AAA CTT CCT GTG CTG ACC AAA TCC ACC GCA ACT GGC ATC ACT GTA TCC GGT GCG CAG TCC TTC AAG CCT GTC GCA TGG CAA CTG GAT AAC GAT GGC AAC AAA GTT AAC GTT GAT AAC CGT TTT GCT ACC GTC ACC CTG TCT GCA ACT ACC GGC ATG AAA CGC GGC GAC AAA ATT TCG TTT GCT GGC GTT AAG TTC CTT GGT CAG ATG GCT AAG AAC GTA CTG GCT CAG GAT GCG ACT TTC TCC GTA GTC CGC GTT GTT GAC GGT ACT CAT GTT GAA ATC ACG CCG AAG CCG GTA GCG CTG GAT GAT GTT TCC CTG TCT CCG GAG CAG CGT GCC TAC GCC AAC GTT AAC ACC TCG CTG GCT GAT GCA ATG GCA GTG AAC ATT CTG AAC GTT AAA GAC GCT CGC ACT AAT GTG TTC TGG GCT GAC GAT GCT ATT CGT ATC GTG TCT CAG CCG ATT CCG GCT AAC CAT GAA CTT TTT GCA GGT ATG AAA ACT ACC TCA TTC AGC ATC CCT GAT GTT GGC CTG AAC GGT ATC TTC GCT ACG CAG GGT GAT ATT TCC ACC CTG TCC GGC CTG TGC CGT ATT GCG CTG TGG TAC GGC GTA AAC GCG ACA CGA CCG GAG GCA ATC GGT GTT GGC CTG

CCT GGT CAG ACT GCG ACT AGT GTG GCG GCG CTG GAA AAA GAA GTT GCC GCC TTG GAG AAG GAG TAG

CP with Q2 (CP-Q2)

ATG GCT TTG AAC GAA GGT CAA ATT GTT ACA CTG GCG GTA GAT GAA ATC ATC GAA ACC ATC TCC GCA ATC ACT CCA ATG GCG CAG AAA GCC AAG AAA TAC ACC CCG CCT GCT GCT TCT ATG CAG CGC TCC AGC AAT ACC ATC TGG ATG CCT GTA GAG CAA GAG TCA CCC ACT CAG GAG GGC TGG GAT TTA ACT GAT AAA GCG ACA GGG TTA CTG GAA CTT AAC GTC GCG GTA AAC ATG GGA GAG CCG GAT AAC GAC TTC TTC CAG TTG CGT GCT GAT GAC TTG CGA GAC GAA ACT GCG TAT CGT CGC CGC ATC CAG TCT GCC GCT CGC AAG CTG GCG AAC AAC GTT GAG TTG AAA GTC GCA AAC ATG GCC GCC GAG ATG GGT TCG CTG GTT ATC ACC TCC CCT GAT GCC ATC GGC ACT AAT ACC GCA GAC GCC TGG AAC TTT GTG GCC GAC GCA GAA GAA ATC ATG TTC TCC CGC GAA CTT AAC CGC GAC ATG GGG ACA TCG TAC TTC TTC AAC CCT CAG GAC TAC AAA AAA GCG GGT TAC GAC CTG ACC AAG CGT GAC ATC TTC GGG CGT ATT CCT GAA GAA GCA TAC CGA GAT GGC ACC ATT CAG CGT CAG GTC GCT GGC TTC GAT GAT GTC CTG CGC TCT CCG AAA CTT CCT GTG CTG ACC AAA TCC ACC GCA ACT GGC ATC ACT GTA TCC GGT GCG CAG TCC TTC AAG CCT GTC GCA TGG CAA CTG GAT AAC GAT GGC AAC AAA GTT AAC GTT GAT AAC CGT TTT GCT ACC GTC ACC CTG TCT GCA ACT ACC GGC ATG AAA CGC GGC GAC AAA ATT TCG TTT GCT GGC GTT AAG TTC CTT GGT CAG ATG GCT AAG AAC GTA CTG GCT CAG GAT GCG ACT TTC TCC GTA GTC CGC GTT GTT GAC GGT ACT CAT GTT GAA ATC ACG CCG AAG CCG GTA GCG CTG GAT GAT GTT TCC CTG TCT CCG GAG CAG CGT GCC TAC GCC AAC GTT AAC ACC TCG CTG GCT GAT GCA ATG GCA GTG AAC ATT CTG AAC GTT AAA GAC GCT CGC ACT AAT GTG TTC TGG GCT GAC GAT GCT ATT CGT ATC GTG TCT CAG CCG ATT CCG GCT AAC CAT GAA CTT TTT GCA GGT ATG AAA ACT ACC TCA TTC AGC ATC CCT GAT GTT GGC CTG AAC GGT ATC TTC GCT ACG CAG GGT GAT ATT TCC ACC CTG TCC GGC CTG TGC CGT ATT GCG

CTG TGG TAC GGC GTA AAC GCG ACA CGA CCG GAG GCA ATC GGT GTT GGC CTG CCT GGT CAG ACT GCG ACT AGT GTG GCG GCG CTG CAG AGC CAA GTG GCG GCG CTT CAA AGT CAG TAA

CP with K2 (CP-K2)

ATG GCT TTG AAC GAA GGT CAA ATT GTT ACA CTG GCG GTA GAT GAA ATC ATC GAA ACC ATC TCC GCA ATC ACT CCA ATG GCG CAG AAA GCC AAG AAA TAC ACC CCG CCT GCT GCT TCT ATG CAG CGC TCC AGC AAT ACC ATC TGG ATG CCT GTA GAG CAA GAG TCA CCC ACT CAG GAG GGC TGG GAT TTA ACT GAT AAA GCG ACA GGG TTA CTG GAA CTT AAC GTC GCG GTA AAC ATG GGA GAG CCG GAT AAC GAC TTC TTC CAG TTG CGT GCT GAT GAC TTG CGA GAC GAA ACT GCG TAT CGT CGC CGC ATC CAG TCT GCC GCT CGC AAG CTG GCG AAC AAC GTT GAG TTG AAA GTC GCA AAC ATG GCC GCC GAG ATG GGT TCG CTG GTT ATC ACC TCC CCT GAT GCC ATC GGC ACT AAT ACC GCA GAC GCC TGG AAC TTT GTG GCC GAC GCA GAA GAA ATC ATG TTC TCC CGC GAA CTT AAC CGC GAC ATG GGG ACA TCG TAC TTC TTC AAC CCT CAG GAC TAC AAA AAA GCG GGT TAC GAC CTG ACC AAG CGT GAC ATC TTC GGG CGT ATT CCT GAA GAA GCA TAC CGA GAT GGC ACC ATT CAG CGT CAG GTC GCT GGC TTC GAT GAT GTC CTG CGC TCT CCG AAA CTT CCT GTG CTG ACC AAA TCC ACC GCA ACT GGC ATC ACT GTA TCC GGT GCG CAG TCC TTC AAG CCT GTC GCA TGG CAA CTG GAT AAC GAT GGC AAC AAA GTT AAC GTT GAT AAC CGT TTT GCT ACC GTC ACC CTG TCT GCA ACT ACC GGC ATG AAA CGC GGC GAC AAA ATT TCG TTT GCT GGC GTT AAG TTC CTT GGT CAG ATG GCT AAG AAC GTA CTG GCT CAG GAT GCG ACT TTC TCC GTA GTC CGC GTT GTT GAC GGT ACT CAT GTT GAA ATC ACG CCG AAG CCG GTA GCG CTG GAT GAT GTT TCC CTG TCT CCG GAG CAG CGT GCC TAC GCC AAC GTT AAC ACC TCG CTG GCT GAT GCA ATG GCA GTG AAC ATT CTG AAC GTT AAA GAC GCT CGC ACT AAT GTG TTC TGG GCT GAC GAT GCT ATT CGT ATC GTG TCT CAG CCG ATT CCG GCT AAC CAT GAA CTT TTT GCA GGT ATG AAA ACT ACC TCA TTC AGC ATC CCT GAT GTT GGC CTG AAC GGT ATC

TTC GCT ACG CAG GGT GAT ATT TCC ACC CTG TCC GGC CTG TGC CGT ATT GCG CTG TGG TAC GGC GTA AAC GCG ACA CGA CCG GAG GCA ATC GGT GTT GGC CTG CCT GGT CAG ACT GCG ACT AGG GTG GCG GCG CTG AAA GAA AAA GTT GCC GCC TTA AAG GAG AAG TAG

SP141

ATG GGC AGC AGC CAT CAC CAT CAT CAC CAC AGC CAG GAT CCC TGG TGC CGC GCG GCA GCA TGT CGC AGC AAT GCC GTA GCA GAA CAG GGC CGC AAG ACT CAG GAG TTT ACC CAG CAA TCA GCG CAA TAC GTC GAA GCT GCC CGC AAA CAC TAT GAC GCG GCG GAA AAG CTC AAC ATC CCT GAC TAT CAG GAG AAA GAA GAC GCA TTT ATG CAA CTG GTT CCG CCT GCG GTT GGG GCC GAC ATT ATG CGC CTG TTC CCG GAA AAG TCC GCC GCG CTC ATG TAT CAC CTG GGG GCA AAC CCG GAG AAA GCC CGC CAG TTA CTG GCG ATG GAT GGG CAG TCC GCG CTG ATT GAA CTC ACT CGA CTA TCC GAA CGC TTA ACT CTC AAG CCT CGC GGT AAA CAA ATC TCT TCC GCT CCC CAT GCT GAC CAG CCT ATT ACC GGT GAT GTC AGC GCA GCA AAT AAA GAT GCC ATT CGT AAA CAA ATG GAT GCT GCT GCG AGC AAG GGA GAT GTG GAA ACC TAC CGC AAG CTA AAG GCA AAA CTT AAA GGA ATC CGA TAA

Amino acid sequences of proteins used in this study:

Note: The bold part in CP-E2, CP-Q2, and CP-K2 sequences corresponds to E2, Q2, and K2 peptides respectively.

CP-E2

MALNEGQIVTLAVDEIIETISAITPMAQKAKKYTPPAASMQRSSNTIWMPVEQESPTQEG WDLTDKATGLLELNVAVNMGEPDNDFFQLRADDLRDETAYRRRIQSAARKLANNVEL KVANMAAEMGSLVITSPDAIGTNTADAWNFVADAEEIMFSRELNRDMGTSYFFNPQDY KKAGYDLTKRDIFGRIPEEAYRDGTIQRQVAGFDDVLRSPKLPVLTKSTATGITVSGAQS FKPVAWQLDNDGNKVNVDNRFATVTLSATTGMKRGDKISFAGVKFLGQMAKNVLAQ DATFSVVRVVDGTHVEITPKPVALDDVSLSPEQRAYANVNTSLADAMAVNILNVKDAR

TNVFWADDAIRIVSQPIPANHELFAGMKTTSFSIPDVGLNGIFATQGDISTLSGLCRIALW

YGVNATRPEAIGVGLPGQTATS**VAALEKEVAALEKE**

CP-Q2

MALNEGQIVTLAVDEIIETISAITPMAQKAKKYTPPAASMQRSSNTIWMPVEQESPTQEG

WDLTDKATGLLELNVAVNMGEPDNDFFQLRADDLRDETAYRRRIQSAARKLANNVEL

KVANMAAEMGSLVITSPDAIGTNTADAWNFVADAEEIMFSRELNRDMGTSYFFNPQDY

KKAGYDLTKRDIFGRIPEEAYRDGTIQRQVAGFDDVLRSPKLPVLTKSTATGITVSGAQS

FKPVAWQLDNDGNKVNVDNRFATVTLSATTGMKRGDKISFAGVKFLGQMAKNVLAQ

DATFSVVRVVDGTHVEITPKPVALDDVSLSPEQRAYANVNTSLADAMAVNILNVKDAR

TNVFWADDAIRIVSQPIPANHELFAGMKTTSFSIPDVGLNGIFATQGDISTLSGLCRIALW

YGVNATRPEAIGVGLPGQTATS**VAALQSQVAALQSQ**

CP-K2

MALNEGQIVTLAVDEIIETISAITPMAQKAKKYTPPAASMQRSSNTIWMPVEQESPTQEG

WDLTDKATGLLELNVAVNMGEPDNDFFQLRADDLRDETAYRRRIQSAARKLANNVEL

KVANMAAEMGSLVITSPDAIGTNTADAWNFVADAEEIMFSRELNRDMGTSYFFNPQDY

KKAGYDLTKRDIFGRIPEEAYRDGTIQRQVAGFDDVLRSPKLPVLTKSTATGITVSGAQS

FKPVAWQLDNDGNKVNVDNRFATVTLSATTGMKRGDKISFAGVKFLGQMAKNVLAQ

DATFSVVRVVDGTHVEITPKPVALDDVSLSPEQRAYANVNTSLADAMAVNILNVKDAR

TNVFWADDAIRIVSQPIPANHELFAGMKTTSFSIPDVGLNGIFATQGDISTLSGLCRIALW

YGVNATRPEAIGVGLPGQTATR**VAALKEKVAALKEK**

SP141

MGSSHHHHHHSQDPWCRAAACRSNAVAEQGRKTQEFTQQSAQYVEAARKHYDAAEK

LNIPDYQEKEDAFMQLVPPAVGADIMRLFPEKSAALMYHLGANPEKARQLLAMDGQSA

LIELTRLSERLTLKPRGKQISSAPHADQPITGDVSAANKDAIRKQMDAAASKGDVETYRK

LKAKLKGIR

Model and Simulation Details

Coarse-graining solvent and ions: The solvent (water) was treated as a continuous medium in the coarse-grained model and its effect was incorporated implicitly by scaling the electrostatic forces on virus-like particles (VLPs) and dendrimers by the relative dielectric permittivity of water ($\epsilon_w = 78.54$). All hydrodynamic interactions were neglected. Similarly, to speed-up the simulations, the effects of the salt ions (NaCl, Sodium Phosphate) were modeled implicitly by introducing the screened Yukawa potential (equation 1 of the main text) characterized by a surface charge parameter q and the Debye length κ^{-1} (that varied between 0.5 and 3 nm over the range of ionic strengths studied). While using a single adjustable parameter q to describe the charged VLP and dendrimer surface enables an effective minimal model representation of the larger-scale VLP assembly phenomena, it is not expected to comprehensively capture the role of neglected effects at the coarse-grained level.[9] These effects include excluded volume effects due to finite ion sizes, electrostatic correlations between ions, and inhomogeneities in the surface charge distribution. Appropriate q values for VLP assembly studies were selected using a combination of experimentally-informed analytical approximations and simulation data-driven approach (see below).

Modeling steric effects: P22 VLPs and G6 PAMAM dendrimers were modeled as rigid spheres interacting sterically via a modified repulsive Lennard-Jones (LJ) potential (equation 2 of the main text). van der Waals attractive forces between particles were neglected as they are much weaker compared to the inter-particle electrostatic attraction at the probed length scales. The addition of peptides on the bare VLP surface is expected to modulate the accessibility and proximity of the dendrimers to the VLP surface. Dendrimers are also relatively deformable and are expected to conform to the VLP surface,[10] which can further alter their steric interaction with the VLPs. These effects were incorporated in the coarse-grained steric potential via the parameter σ_{hc}. σ_{hc} was chosen to be 6.7 nm for all the three VLP variants. This value allows for a VLP-dendrimer closest approach distance of ≈ 30.7 nm, which is ≈ 0.6 nm smaller than the VLP-dendrimer touch-

ing distance, in agreement with previously reported SAXS-based experimental assessments of the nearest neighbor spacing between two P22-E2 VLPs in an ordered array bridged by an interstitial dendrimer[3] (shown to be approximately 61.5 nm). We note that for the chosen $\sigma_{\text{hc}} = 6.7$ nm, the dendrimer-dendrimer steric repulsion reduced to the standard LJ potential (as dendrimer diameter $\sigma_d = 6.7$ nm).

Simulations show the number of condensed dendrimers to be critical to both the order acquired and assembly itself. If under-condensation occurs, assembly is severely diminished; if there is over-condensation, assembly into amorphous aggregates occurs. The equilibrium number of condensed dendrimers per VLP depends on the net VLP-dendrimer interaction. Decreasing σ_{hc} increases the steric repulsion, modulating the VLP-dendrimer potential and thus the number of condensed dendrimers at a given ionic strength. A plot of the net VLP-dendrimer interaction potential (including electrostatic interaction) with curves corresponding to different values of σ_{hc} is shown in Fig. S5. Changing σ_{hc} tunes the value of the potential minimum and the average distance of closest approach.

Modeling electrostatic interactions: VLPs were modeled as uniformly charged spheres of radius $a = 28$ nm that electrostatically interact with other VLPs and dendrimers via a screened Yukawa potential (Equation 1 of the main text) characterized by a surface charge parameter q_v and the Debye length κ^{-1}. P22-E2, P22-Q2, and P22-K2 exhibited a ζ potential of -30.4 mV, -23.6 mV, and -12.8 mV at 41.1 mM, pH = 7 respectively. Given these experimental measurements were performed close to the lowest ionic strength I, ζ for higher I values is expected to be further reduced. As $a \gg \kappa^{-1}$ and ζ values are small ($\lesssim 1.2k_BT/e$) over a wide range of I values, an approximate estimate for the net surface charge parameter q_v was obtained using the relation $q_v = \tilde{a}(1+\kappa\tilde{a})\zeta/l_B$.[11] Here $\tilde{a}$ is the radius of the VLP out to the shear surface associated with the ζ potential measurement, often approximated as $\tilde{a} = a + \kappa^{-1}$ (note $a \gg \kappa^{-1}$). The linear correlation between q_v and ζ, as outlined in this equation, was assumed; accordingly, q_v for P22-Q2 and P22-K2 were chosen to be approximately 4/5 and 2/5 of the q_v value for P22-E2.

To estimate q_v for P22-E2, a number of factors were considered. First, an upper bound on the value of q_v was established to be $\bar{q}_v \approx -3300e$ from sequence analysis assuming all residues are charged.[12] Next, q_v was correlated with ζ measurements of P22-E2 for multiple values of I to estimate plausible values for surface charge $\tilde{q}_v$ following $\tilde{q}_v = \tilde{a}(1 + \kappa\tilde{a})\zeta/l_B$. Both $\zeta = -30.4$ mV at 41.1 mM and $\zeta = -13.5$ mV at 206 mM yielded $\tilde{q}_v \approx -1000e$. Utilizing $\bar{q}_v$ and $\tilde{q}_v$ as input, a sweep of q_v values between $-500e$ and $-3300e$ was performed (for different dendrimer surface charge parameters; see below), and the P22-E2 VLP assembly for a range of I was monitored. $q_v \approx -1500e$ produced the best alignment with experimental data near ionic strength threshold for the bulk assembly of P22-E2. Using $q_v = -1500e$ for P22-E2 and the aforementioned linear correlation between q_v and ζ, q_v values for P22-Q2 and P22-K2 VLPs were chosen to be $-1200e$ and $-600e$ respectively.

G6 PAMAM dendrimers were modeled as uniformly charged spheres of radius $a_d = 3.35$ nm and effective surface charge q_d. Unlike VLPs, dendrimers exhibit a dendritic topology and are small ($a_d \sim \kappa^{-1}$), making estimation of q_d more challenging and ambiguous. It is expected that a significant fraction of the 256 terminal amine groups of a G6 PAMAM dendrimer will be dissociated at pH = 7.[13,14] However, strong counterion condensation is expected to occur in such charged dendrimer systems, leading to significant charge renormalization effects.[13,15] Experimental and analytical studies produce an estimate for G6 PAMAM dendrimers at $I = 1$ mM of $q_d \approx 15e$ in experiments, and $q_d \approx 35e$ from theoretical arguments;[13] these are also similar to those obtained for a different type of dendrimer with a comparable excess of terminal amines.[15] With these inputs in mind, a sweep over q_d between $20e$ and $45e$ was performed and the P22-E2 VLP assembly was monitored as a function of I ranging from 10 mM to 350 mM. The assembly characteristics were found to be in highest alignment with experiments for $q_v \approx -1500e, q_d \approx 35e$. Thus, for all VLP assembly studies, q_d was chosen to be $35e$. Again, charge renormalization effects as a function of ionic strength were neglected given surface roughness and other considerations limiting the capacity to theoretically estimate this variability.

A sweep over a larger q_v range yielded more VLP, dendrimer combinations that replicated the

experimentally observed P22-E2 assembly trends (e.g, $q_v \approx -2600e, q_d \approx 20e$) indicating that some ambiguity and variability exists in selecting effective charge parameters to describe coarse-grained VLP and dendrimer surfaces. These different combinations produced similar net VLP-dendrimer interaction potential (including steric interaction) of $-5\,k_BT$ at the distance of closest approach for the ionic strength threshold corresponding to the bulk assembly of P22-E2, making this potential a key feature of the minimal model representation.

Simulation details: Starting from a random configuration, all simulations were performed in an NVT ensemble within a cubic, periodic simulation box. A Nose-Hoover thermostat was employed to keep the temperature fixed at $T = 298$ K. The thermostat timescale (damping parameter) was $\tau_t = 100\Delta t$, where $\Delta t \approx 4$ ps denotes the simulation timestep. At periodic intervals during the simulation, the position coordinates of the dendrimers and VLPs were stored for post-processing to compute structural quantities such as the pair correlation functions, VLP-bound dendrimer fractions, as well as kinetic information. The majority of simulations reported used 108 VLPs and 108,000 dendrimers. Additional simulations with $\approx 5\times$ more number of particles were performed to examine finite size effects at the ionic strength thresholds for each VLP variant. Simulations were implemented in the Large-scale Atomic/Molecular Massively Parallel Simulator software (LAMMPS, 31Mar17 build)[16] on Indiana University's Big Red II supercomputer. A typical simulation took approximately 200 hours to complete using MPI acceleration between 32 Cray XE6 nodes.

Post-processing: Post-processing was done using a combination of code written in C++ and Wolfram Research's Mathematica 11.2.[17] The radius of gyration was computed in Mathematica 11.2 by first 'crawling' through all VLPs to identify the largest cluster (a contingent subset within $1.25\sigma_v$ of one another), then accounting for periodicity in all directions and computing the following:

$$R_g = \sqrt{\frac{1}{N}\sum_{k=1}^{N}(r_k - \bar{r})^2}, \tag{5}$$

where N is the total number of VLPs in the cluster, r_k is the position vector of the k^{th} VLP, and $\bar{r}$ is the mean position of all VLPs in the cluster.

VLP-VLP pair correlation functions were computed taking account of periodicity of the box and were found to be convergent using a bin width of $\delta r = 0.005\sigma_v = 0.28$ nm, where σ_v is the VLP diameter. To assess the number of VLP-bound dendrimers, a nearest neighbor algorithm with fixed-distance cutoff was used with the fixed distance of $1.05(\sigma_v + \sigma_d)/2$, that is equal to five percent beyond the touching distance of the particles.[18]

References

(1) Servid, A.; Jordan, P.; ONeil, A.; Prevelige, P.; Douglas, T. Location of the bacteriophage P22 coat protein C-terminus provides opportunities for the design of capsid-based materials. *Biomacromolecules* **2013**, *14*, 2989–2995.

(2) Kang, S.; Uchida, M.; ONeil, A.; Li, R.; Prevelige, P. E.; Douglas, T. Implementation of p22 viral capsids as nanoplatforms. *Biomacromolecules* **2010**, *11*, 2804–2809.

(3) Uchida, M.; McCoy, K.; Fukuto, M.; Yang, L.; Yoshimura, H.; Miettinen, H. M.; LaFrance, B.; Patterson, D. P.; Schwarz, B.; Karty, J. A.; Prevelige, P. E.; Lee, B.; Douglas, T. Modular Self-Assembly of Protein Cage Lattices for Multistep Catalysis. *ACS Nano* **2018**, *12*, 942–953, DOI: 10.1021/acsnano.7b06049, PMID: 29131580.

(4) Kostiainen, M. A.; Hiekkataipale, P.; Laiho, A.; Lemieux, V.; Seitsonen, J.; Ruokolainen, J.; Ceci, P. Electrostatic assembly of binary nanoparticle superlattices using protein cages. *Nature nanotechnology* **2013**, *8*, 52.

(5) McCoy, K.; Uchida, M.; Lee, B.; Douglas, T. Templated Assembly of a Functional Ordered Protein Macromolecular Framework from P22 Virus-like Particles. *ACS nano* **2018**, *12*, 3541–3550.

(6) Li, T.; Senesi, A. J.; Lee, B. Small angle X-ray scattering for nanoparticle research. *Chemical reviews* **2016**, *116*, 11128–11180.

(7) Hummer, D. R.; Heaney, P. J.; Post, J. E. In situ observations of particle size evolution during the hydrothermal crystallization of TiO2: a time-resolved synchrotron SAXS and WAXS study. *Journal of Crystal Growth* **2012**, *344*, 51–58.

(8) Langford, J. I.; Wilson, A. Scherrer after sixty years: a survey and some new results in the determination of crystallite size. *Journal of Applied Crystallography* **1978**, *11*, 102–113.

(9) Hartkamp, R.; Biance, A.-L.; Fu, L.; Dufrêche, J.-F.; Bonhomme, O.; Joly, L. Measuring surface charge: why experimental characterization and molecular modeling should be coupled. *Current Opinion in Colloid & Interface Science* **2018**,

(10) Li, J.; Piehler, L.; Qin, D.; Baker, J.; Tomalia, D.; Meier, D. Visualization and characterization of poly (amidoamine) dendrimers by atomic force microscopy. *Langmuir* **2000**, *16*, 5613–5616.

(11) Hunter, R. J. *Zeta potential in colloid science: principles and applications*; Academic press, 2013; Vol. 2.

(12) Božič, A. L.; Šiber, A.; Podgornik, R. How simple can a model of an empty viral capsid be? Charge distributions in viral capsids. *Journal of biological physics* **2012**, *38*, 657–671.

(13) Pericet-Camara, R.; Papastavrou, G.; Borkovec, M. Effective charge of adsorbed poly (amidoamine) dendrimers from direct force measurements. *Macromolecules* **2009**, *42*, 1749–1758.

(14) Maiti, P. K.; Messina, R. Counterion distribution and ζ-potential in PAMAM dendrimer. *Macromolecules* **2008**, *41*, 5002–5006.

(15) Xu, X.; Ran, Q.; Haag, R.; Ballauff, M.; Dzubiella, J. Charged dendrimers revisited: Effective charge and surface potential of dendritic polyglycerol sulfate. *Macromolecules* **2017**, *50*, 4759–4769.

(16) Plimpton, S. Fast Parallel Algorithms for Short-Range Molecular Dynamics. *Journal of Computational Physics* **1995**, *117*, 1–19, DOI: https://doi.org/10.1006/jcph.1995.1039.

(17) Wolfram Research Inc., Mathematica, Version 11.2. 2017; Champaign, IL.

(18) van Meel, J. A.; Filion, L.; Valeriani, C.; Frenkel, D. A parameter-free, solid-angle based, nearest-neighbor algorithm. *The Journal of chemical physics* **2012**, *136*, 234107.

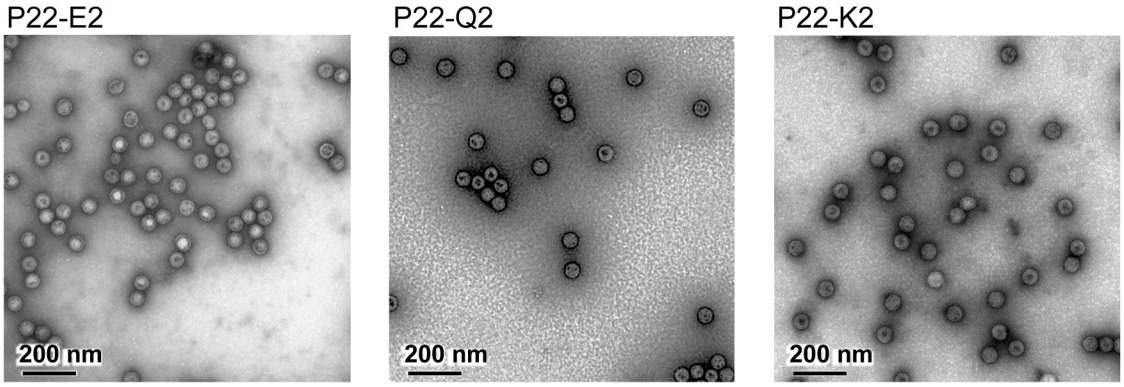

Figure S1: TEM images of P22-E2, P22-Q2 and P22-K2 VLPs. All the VLP constructs assembled into capsid structures with diameters of about 55 nm regardless of the modifications to the coat proteins (CPs), indicating that the genetic fusion of the extra peptide (i.e. (VAALEKE)2, (VAALQSQ)2, or (VAALKEK)2)) at the C-terminus of the CP did not interfere with the self-assembly of the CP subunits into the VLP capsids. The samples were stained with 2% uranyl acetate.

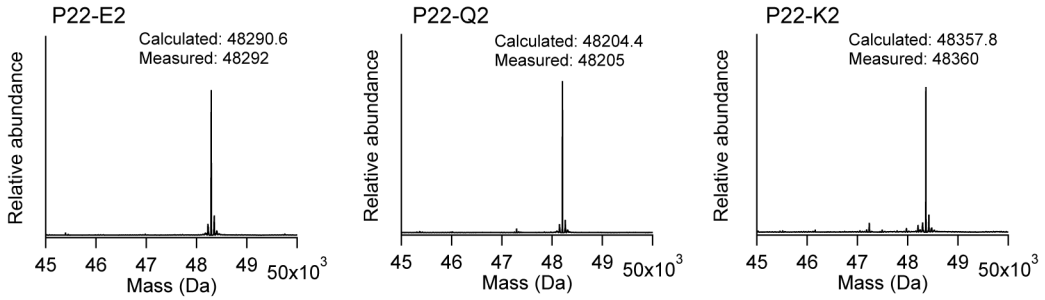

Figure S2: Deconvoluted mass analyses of CP (coat protein) mutants fused with E2 (left), Q2 (center), or K2 (right) mutants. The observed molecular weight of all three mutants are similar and agreed well with the calculated mass of each CP. Each P22 variant is composed of 420 copies of a CP mutant subunit.

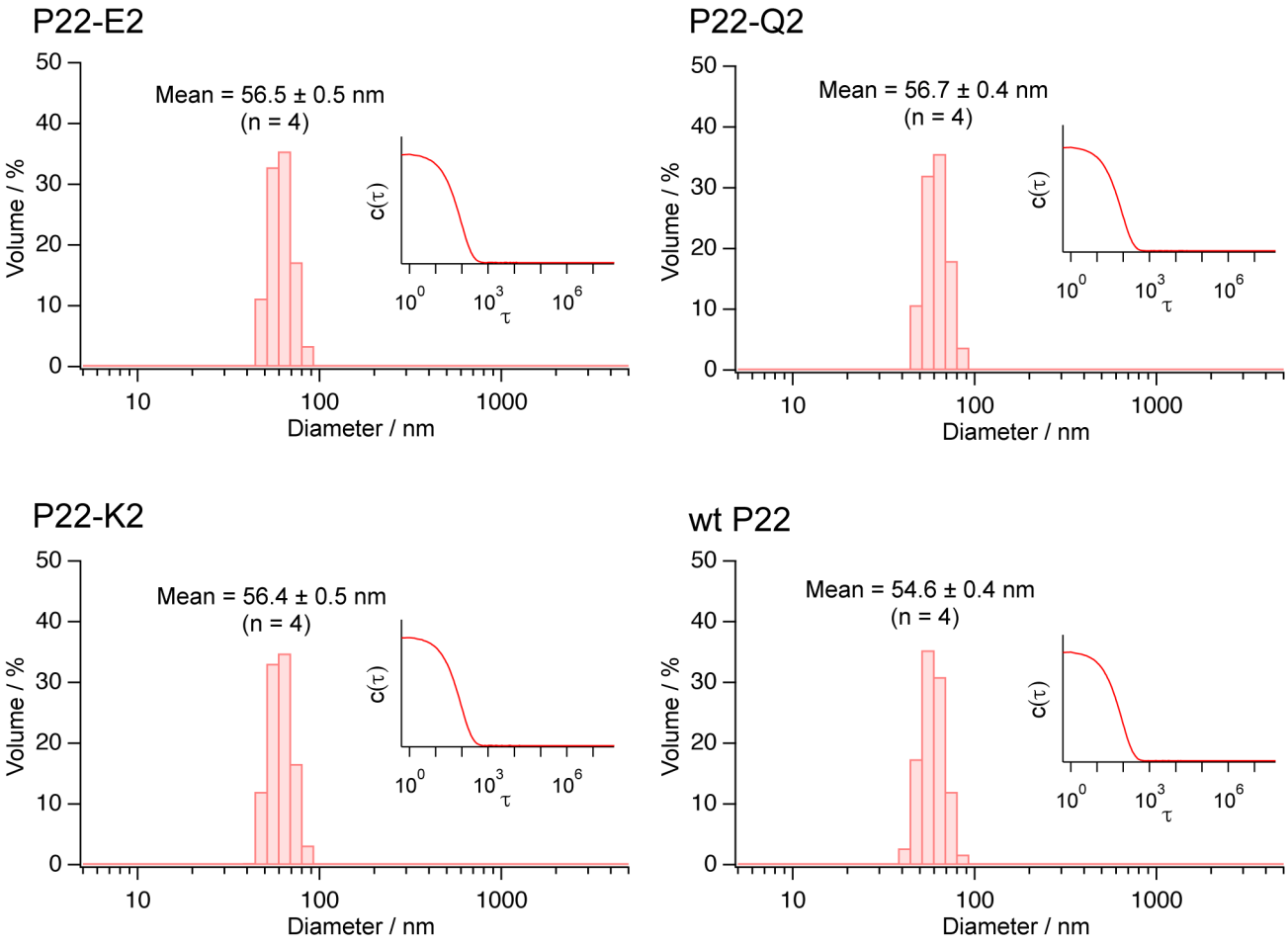

Figure S3: Volume-averaged hydrodynamic diameter of P22-E2, P22-Q2, P22-K2 and wtP22 VLPs measured with DLS and corresponding correlation functions (inset). Hydrodynamic diameters of P22-E2, P22-Q2 and P22-K2 were nearly identical to each other and about 2 nm larger than that of wtP22. Because up to 420 copies of E2, Q2 and K2 peptide could be presented on the exterior surface of the P22-E2, P22-Q2 and P22-K2 VLPs, respectively, it is reasonable to expect these mutants to have slightly larger diameter compared to wtP22 VLP. The mean and standard deviation for each variant was obtained from four repeated measurements. The size distribution histograms and corresponding correlation functions shown here are representative of the four measurements. The measurements were conducted at 25°C.

a

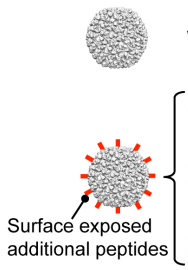

	Additional peptide	Hydrodynamic diameter /nm	Zeta potential / mV	Threshold ionic strength (I_T) / mM
wtP22	-	54.6 ± 0.4	-30.7 ± 2.3	247
P22-E2	$(VAALEKE)_2$	56.5 ± 0.5	-30.4 ± 2.8	247
P22-Q2	$(VAALQSQ)_2$	56.7 ± 0.4	-23.6 ± 2.0	123
P22-K2	$(VAALKEK)_2$	56.4 ± 0.5	-12.8 ± 2.1	61.7

b

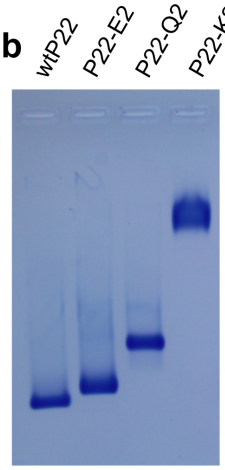

Figure S4: Summary of P22 VLP variants and assessment of their surface charges. (a) Table showing the peptide added to the C-terminus of each P22 variant (second column), the resulting hydrodynamic diameter (third column), zeta potential at pH 7.0 and ionic strength of 41.1 mM ($n = 4$ measurements); the final column shows the threshold ionic strength I_t above which the dendrimer-mediated assembly of VLPs into ordered arrays was not observed. Wild type P22 showed a negative surface charge of -30.7 mV. P22-Q2 exhibited a less negative surface charge than wtP22 and P22-K2 exhibited the least negative surface charge. P22-E2 showed a negative surface charge almost identical to wtP22, suggesting that the negatively charged E2 peptide does not alter the overall surface charge of the VLP. The zeta potential estimates were taken at $15°$C. (b) Native agarose gel electrophoresis of wtP22, P22-E2, P22-Q2 and P22-K2 VLPs. All samples moved toward the anode, which indicates net negative surface charge. Because the molecular weight and hydrodynamic diameter of P22-E2, P22-Q2 and P22-K2 are almost identical (Fig. S2 and Fig. S3), the mobility largely depends on their surface charge, indicating that P22-E2 and P22-K2 are the most and least negatively charged, respectively. The migration distance of wtP22 was slightly larger than that of P22-E2 despite the zeta potential of the two samples being nearly identical. This is likely due to the smaller size of wtP22 compared to P22-E2.

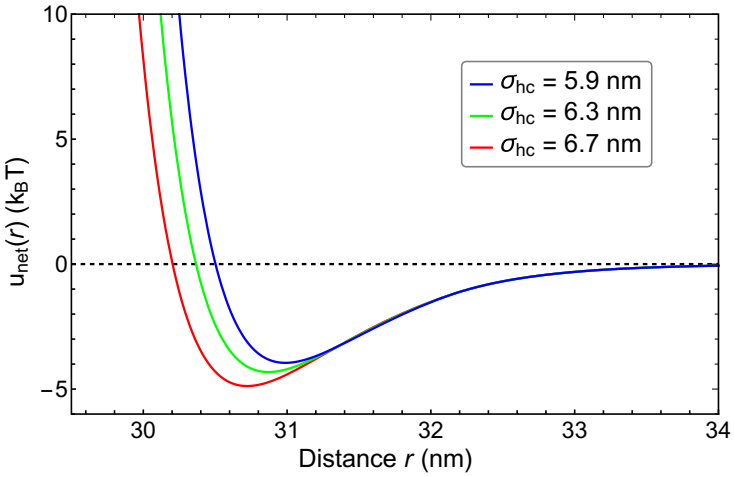

Figure S5: Net VLP-dendrimer potential, $u_{\text{net}}(r) = u_{\text{LJ}}(r) + u_{\text{E}}(r)$, for different values of σ_{hc} at the ionic strength threshold of 225 mM for the P22-E2 VLP system. Decreasing σ_{hc} increases steric repulsion and thus decreases the extent to which the dendrimer may approach the VLP. It can be seen that the distance of closest approach at which the energy minimum occurs rises as σ_{hc} is decreased, with the red curve calibrated using experimental nearest-neighbor distance between two P22-E2 VLPs bridged by a dendrimer in an ordered array.

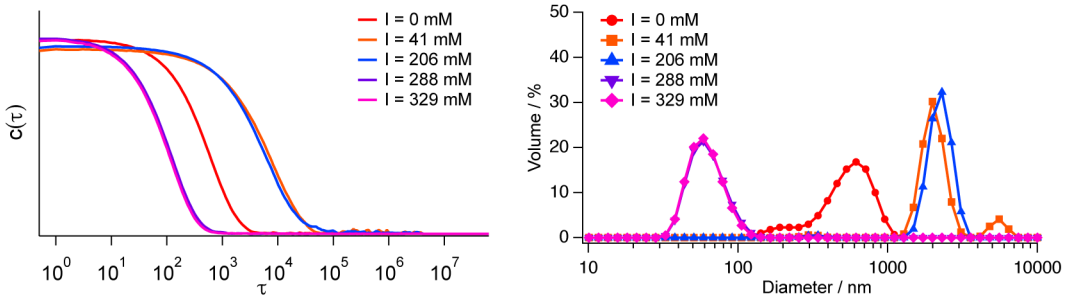

Figure S6: Correlation functions (left) and corresponding volume-averaged hydrodynamic diameter distributions (right) from DLS measurements of P22-E2 assembly when P22-E2 VLPs were mixed with 1000 PAMAM G6 dendrimers per VLP at different solution ionic strength I. For I between 41 and 247 mM, large assemblies of VLPs with aggregate diameter of a few micrometers were formed. For $I = 0$ mM solution, P22-E2 VLPs assembled into arrays but the size was significantly smaller. Above the threshold ionic strength (247 mM), the measured size was around 60 nm, indicating that P22-E2 VLPs were mono-dispersed in the solution and did not form large aggregates.

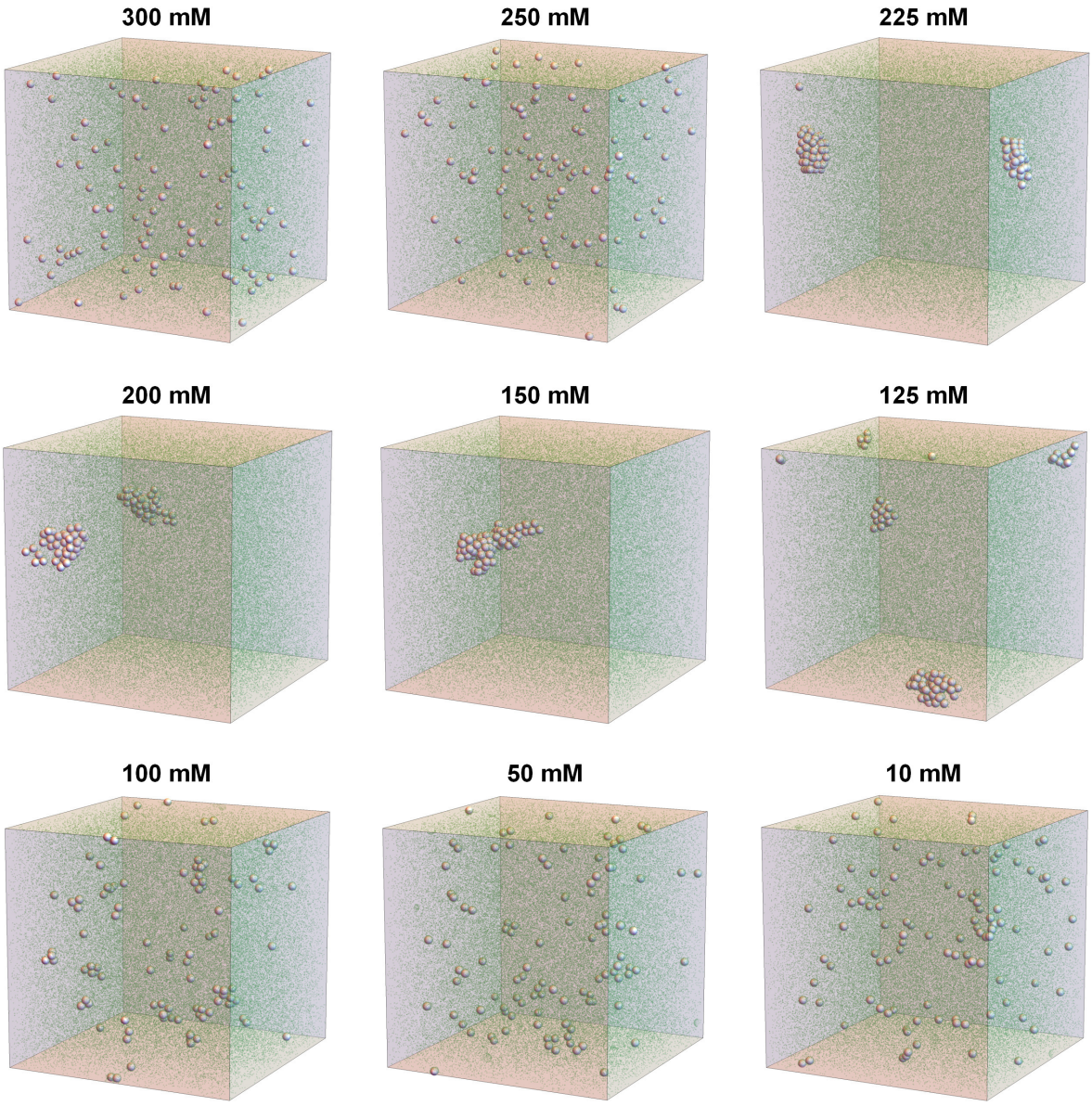

Figure S7: Representative snapshots of typical steady-state configurations of the P22-E2 system; silver spheres are VLPs and smaller green spheres are dendrimers. Ionic strength I decreases from top to bottom, and left to right. An abrupt transition from a suspension of dispersed particles (at $I = 250$ mM) to an ordered, assembled array (at $I = I_t \approx 225$ mM) is observed. As I is reduced further, the clusters become amorphous and elongated, eventually ceasing to assemble.

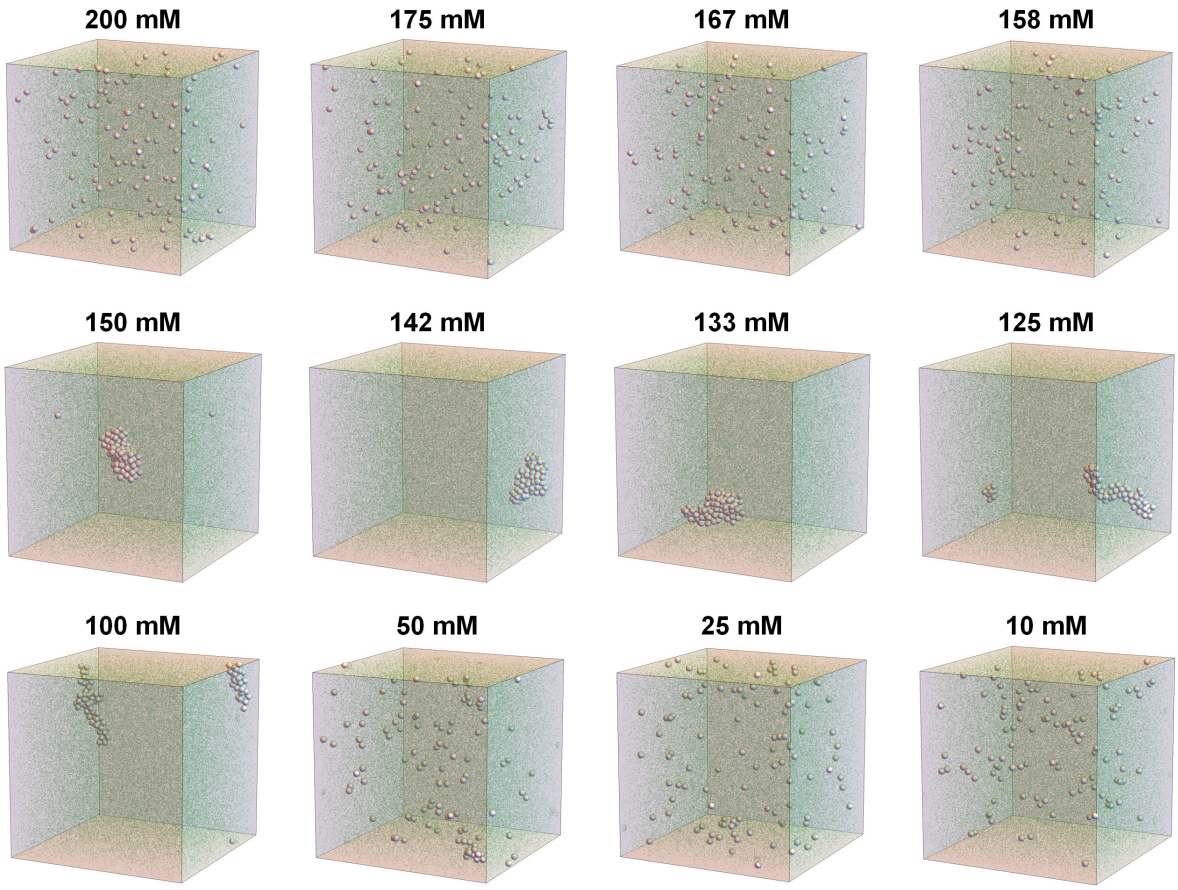

Figure S8: Representative snapshots of typical steady-state configurations of the P22-Q2 system; silver spheres are VLPs and smaller green spheres are dendrimers. Ionic strength I decreases from top to bottom, and left to right. An abrupt transition from a suspension of dispersed particles (at $I = 158$ mM) to an ordered, assembled array (at $I = I_t \approx 150$ mM) is observed. As I is reduced further, the clusters become amorphous and elongated, eventually ceasing to assemble.

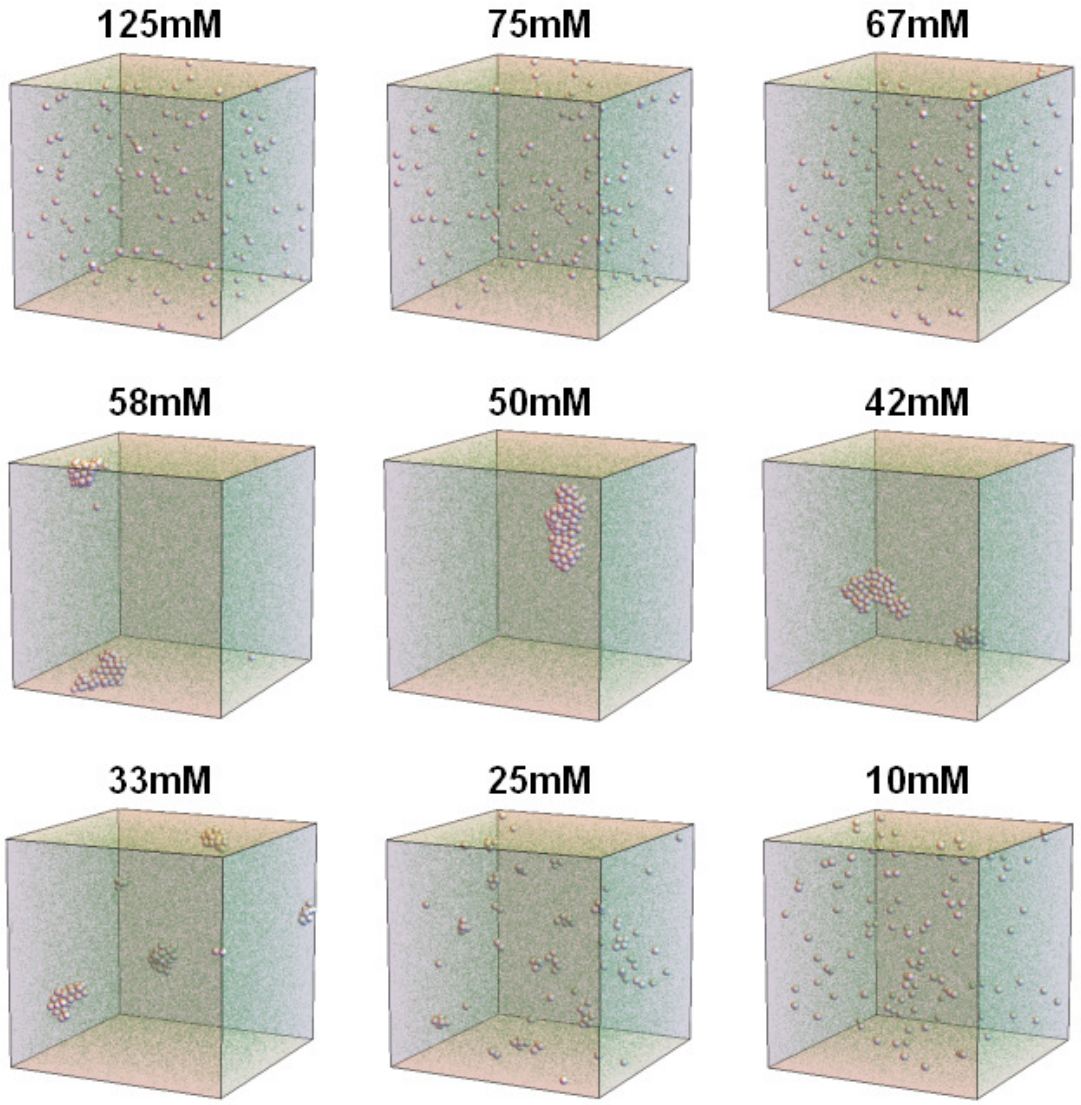

Figure S9: Representative snapshots of typical steady-state configurations of the P22-K2 system; silver spheres are VLPs and smaller green spheres are dendrimers. Ionic strength I decreases from top to bottom, and left to right. An abrupt transition from a suspension of dispersed particles (at $I = 67$ mM) to an ordered, assembled array (at $I = I_t \approx 58$ mM) is observed. As I is reduced further, the clusters become increasingly amorphous and disconnected, eventually ceasing to assemble.

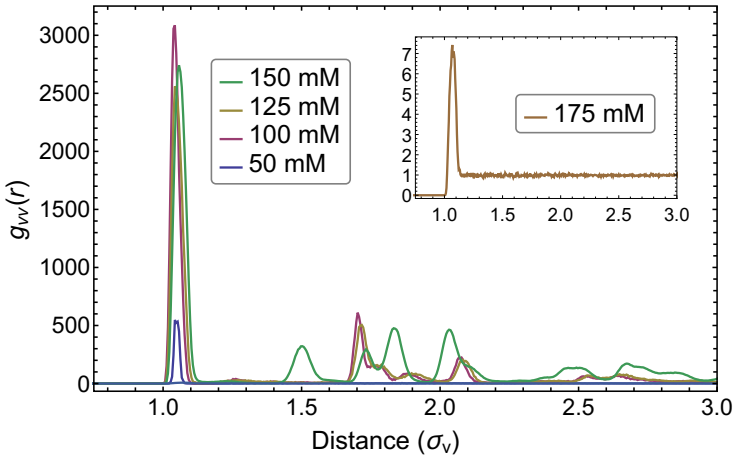

Figure S10: The VLP-VLP pair correlation functions for P22-Q2 system at different ionic strength I. Above the ionic strength threshold of $I_t \approx 150$ mM, the system is a weakly correlated solution of dispersed VLPs (inset); for $I \lesssim I_t$, an abrupt transition to an ordered array of VLPs is observed. Long-range order is diminished as I is reduced further.

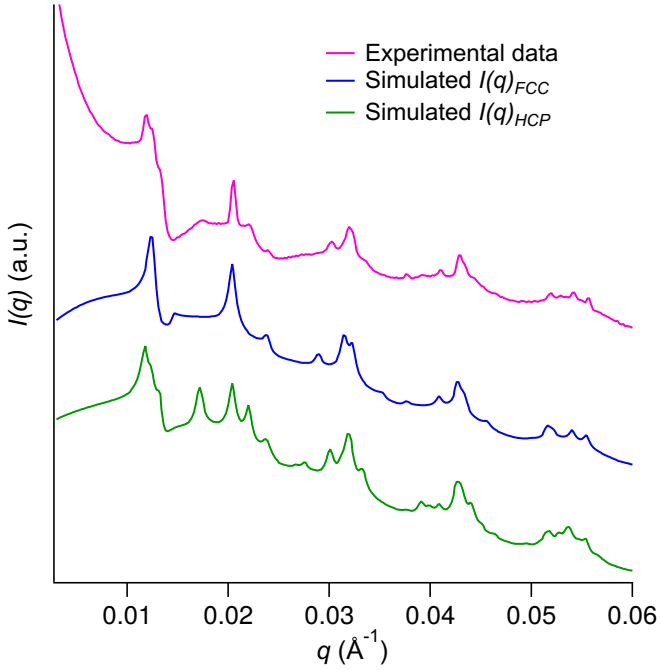

Figure S11: Comparison of experimental SAXS intensity $I(q)$ and theoretical plots of ideal FCC and HCP lattices. The lattice constant for FCC is 87.0 nm. HCP lattice constants are $a = 61.5$ nm and $c = 101.1$ nm. Data are scaled arbitrarily for visual clarity. This data shows the experimental results exhibiting features corresponding to both FCC and HCP lattices. This data is adapted from a previous publication.[3]

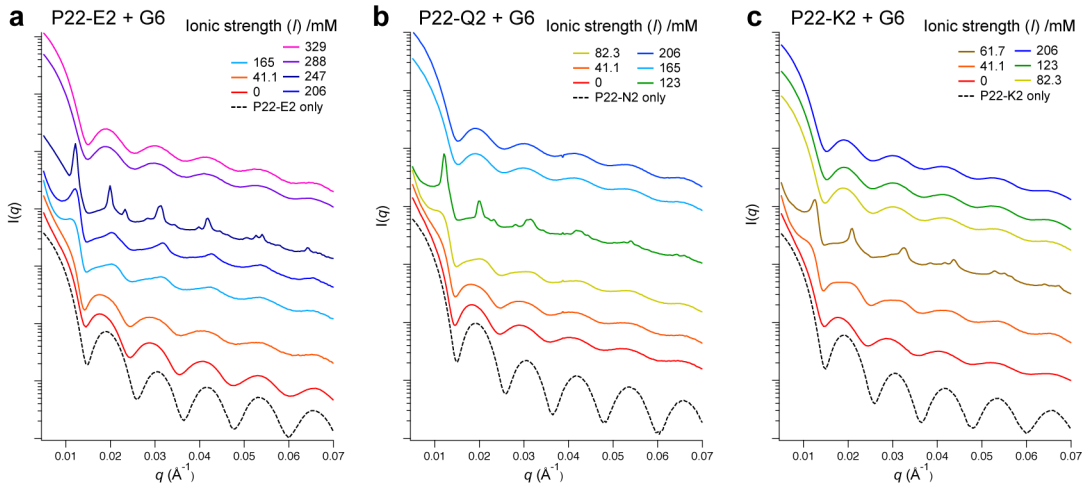

Figure S12: Measured SAXS patterns, $I(q)$ versus q, of (a) P22-E2, (b) P22-Q2, and (c) P22-K2 mixed with G6 dendrimer under various ionic strength conditions. Plots are vertically offset for clarity.

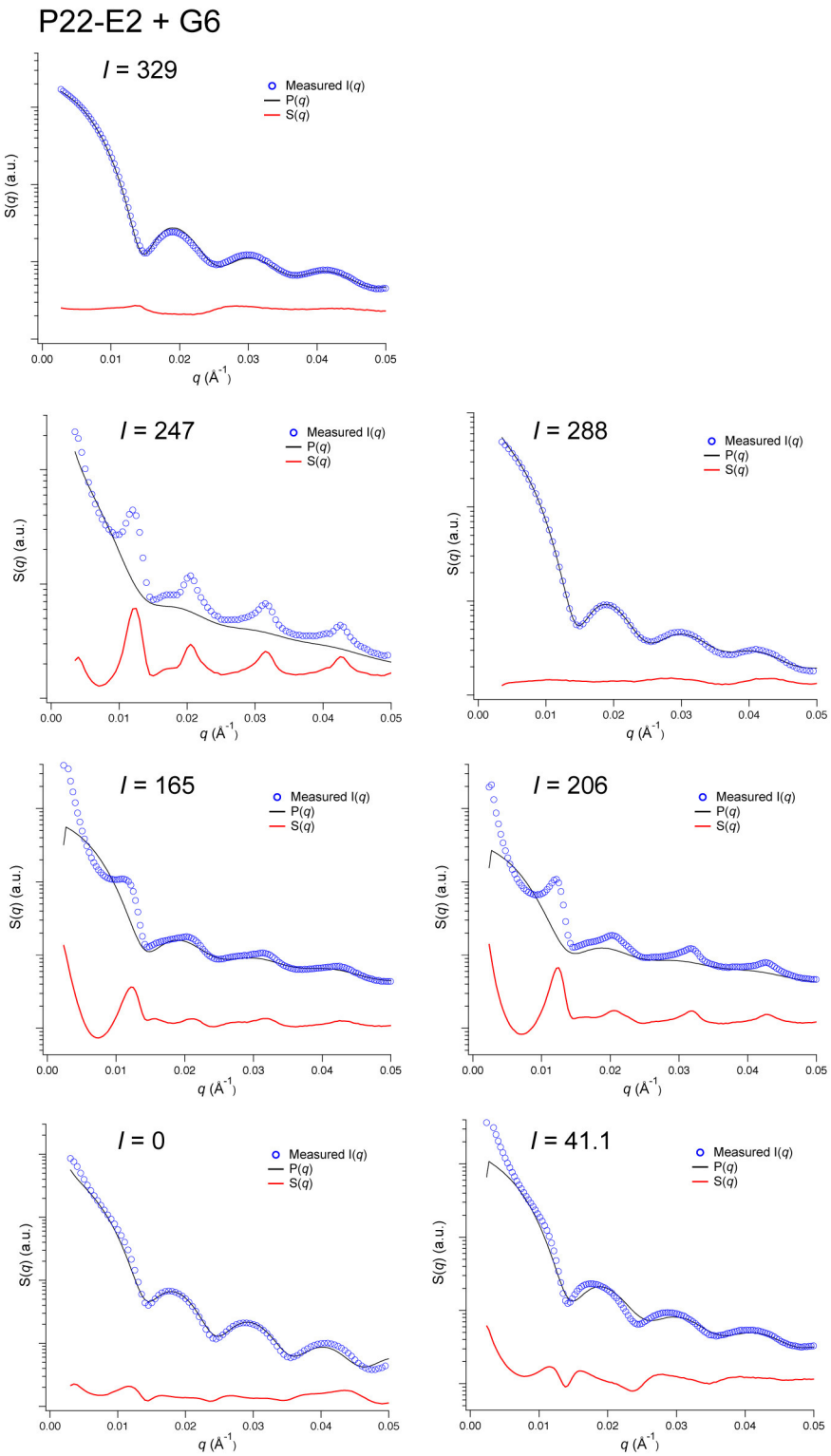

Figure S13: Plots of measured $I(q)$, modeled $P(q)$ and extracted $S(q)$ SAXS data. In all plots, the blue trace is the experimentally obtained $I(q)$ of each sample, and the black trace is the modeled form factor $P(q)$. The structure factor $S(q)$ (red trace) was obtained by dividing $I(q)$ by $P(q)$. The $S(q)$ plots are vertically offset for clarity.

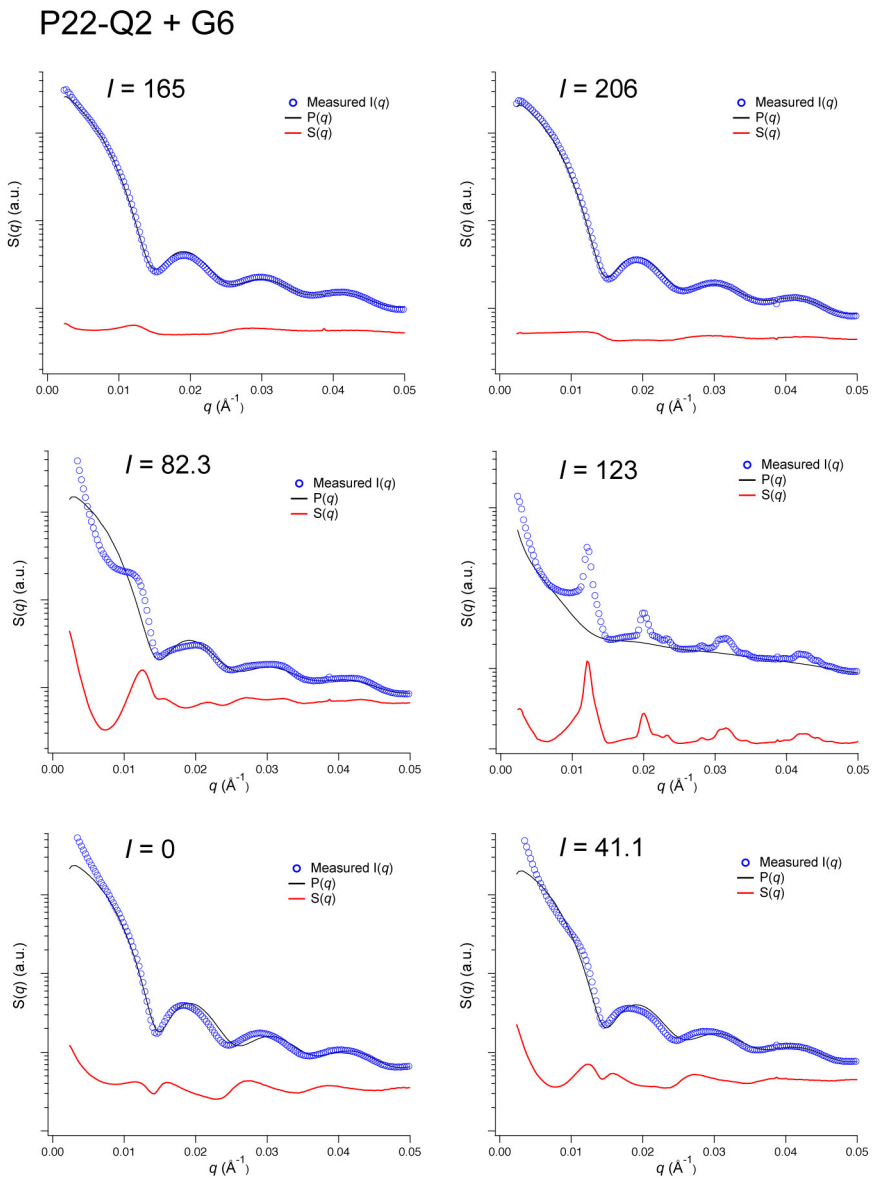

Figure S14: Continuation of Figure S13 for P22-Q2 assembly.

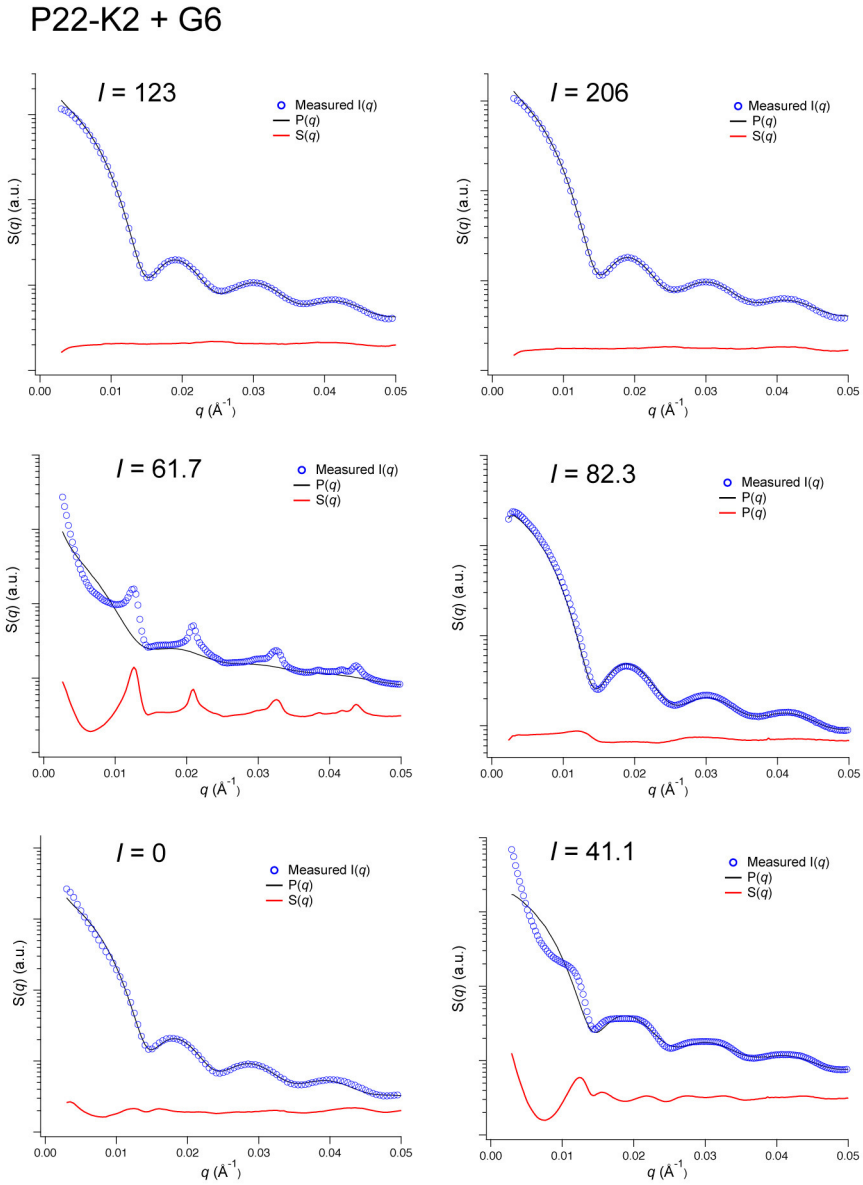

Figure S15: Continuation of Figure S13 for P22-K2 assembly.

P22-E2 + G6

I / mM	Δq_{samp} / Å	Estimated domain size / nm
0	0.00369	153.3
41.1	0.00329	171.8
165	0.00223	260.1
206	0.00175	337.8
247	0.00081	699.4
288	No Assembly	-
329	No Assembly	-

P22-Q2 + G6

I / mM	Δq_{samp} / Å	Estimated domain size / nm
0	0.00379	149.3
41.1	0.00339	167.0
82.3	0.00282	200.8
123	0.00100	564.6
165	No Assembly	-
206	No Assembly	-

P22-K2 + G6

I / mM	Δq_{samp} / Å	Estimated domain size / nm
0	0.00383	147.7
41.1	0.00298	189.7
61.7	0.00141	401.3
82.3	No Assembly	-
123	No Assembly	-
206	No Assembly	-

Figure S16: The full width at half maximum (FWHM) of the resolution-corrected, first-order diffraction peak and estimated domain size of arrays assembled from P22 variants and G6 dendrimers. The domain sizes of the assembled arrays increased with increasing ionic strength until the latter exceeded the threshold ionic strength for each P22 variant.

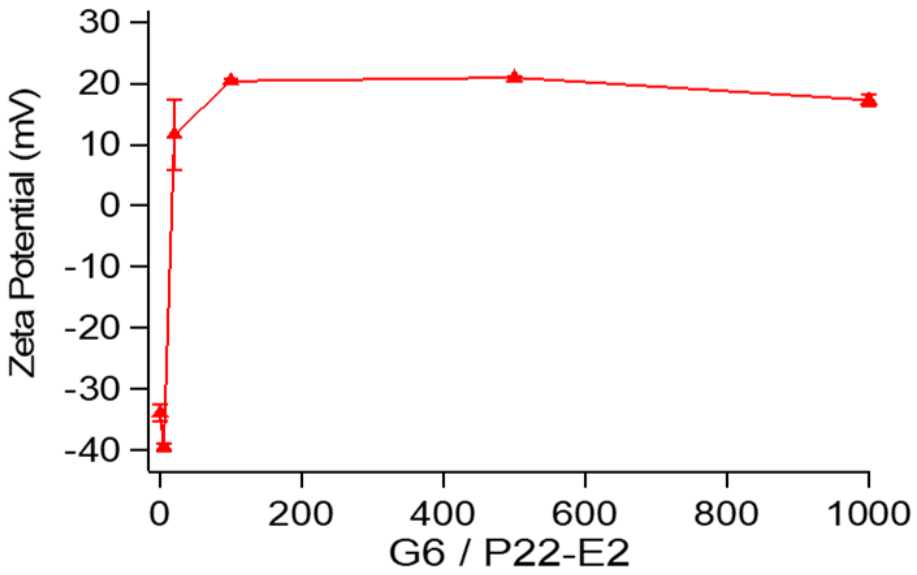

Figure S17: Zeta potential of P22-E2 arrays as a function of G6 dendrimer concentration c_d (measured as the number of dendrimers per P22-E2 VLP) at a low ionic strength of 10 mM ($n = 3$ measurements). The zeta potential of each P22-E2 without G6 was approximately -33 mV. When mixed with G6 dendrimer at $c_d = 5$, the zeta potential of the assembled array stayed negative at -39 mV. The zeta potential of the assembly shifted to a positive value (11 mV) when P22-E2 was mixed with G6 at a concentration of $c_d = 20$, and it reached to around 20 mV at $c_d = 100$. This charge inversion is likely due to over-condensation of G6 dendrimers on the VLP surface, in alignment with the predictions of the computational model.

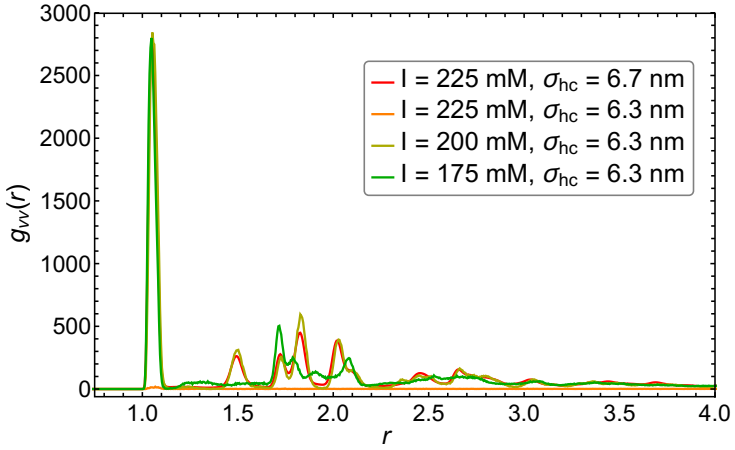

Figure S18: VLP-VLP pair correlation functions showing that increasing VLP-dendrimer steric repulsion (decreasing σ_{hc}) shifts the ionic strength threshold I_t downward. The P22-E2 ordered array (using $\sigma_{\text{hc}} = 6.7$ nm) with threshold $I_t = 225$ mM is shown for reference (red). The increased steric repulsion (for VLP systems with $\sigma_{\text{hc}} = 6.3$ nm) requires a stronger VLP-dendrimer electrostatic attraction to form the ordered array, lowering the ionic strength threshold downward to $I_t = 200$ mM. Further lowering of the ionic strength for the $\sigma_{\text{hc}} = 6.3$ nm system leads to a decrease in the long-range order.

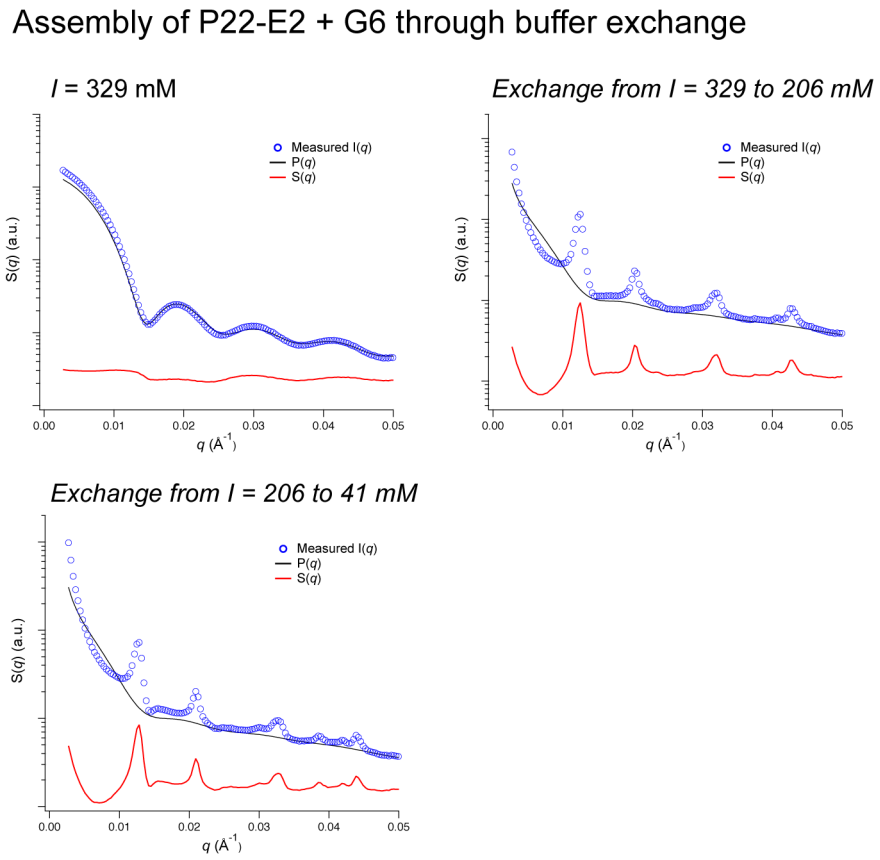

Figure S19: Continuation of Figure S13 during dialysis into lower salt conditions from above the ionic strength threshold I_t (top left), to at I_t (top right), and then at an ionic strength significantly below I_t (bottom).

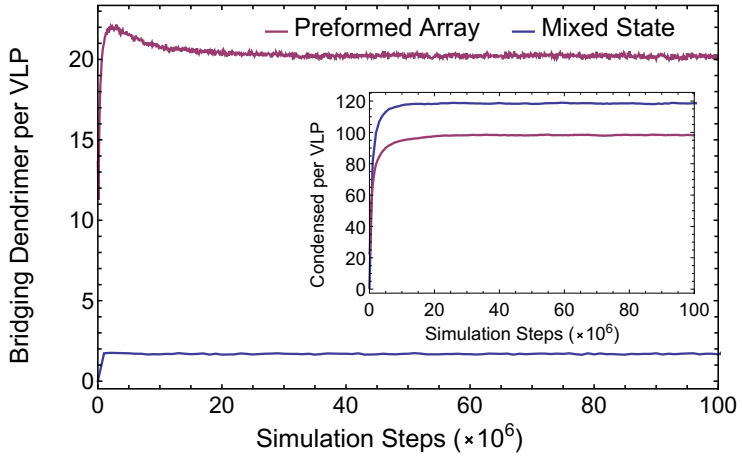

Figure S20: Simulated number of bridging dendrimers N_b per P22-E2 VLP at ionic strength $I = 50$ mM as a function of simulation steps (10^6 steps correspond to ≈ 1 microseconds). Blue curve shows the result for an initially randomly mixed state of VLPs and dendrimers at $I = 50$ mM. Purple curve shows the data for a system initially assembled into an ordered array at $I = I_t \approx 225$ mM and then dialysed to $I = 50$ mM. The ordered structure for the dialysed, preformed array (purple) persisted under low ionic strengths as N_b equilibrated around ≈ 20 (starting at $N_b(0) \approx 12$), but the randomly mixed state (blue) exhibited no ordered assembly due to the lack of bridging dendrimers ($N_b < 2$). Inset shows N_c, the corresponding number of condensed dendrimers per P22-E2 VLP for the two systems. The superlattice persisted despite exhibiting $N_c \sim 100$.

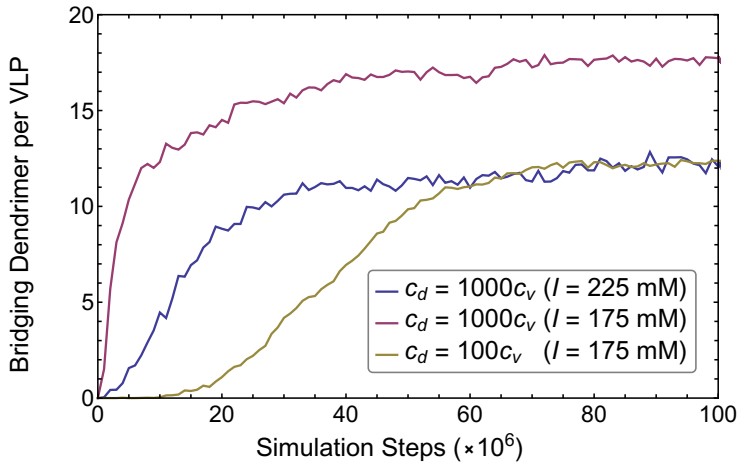

Figure S21: Number of bridging dendrimers N_b for the P22-E2 system where assembly into ordered structures was observed. Curves with different ionic strength I and dendrimer concentration c_d are shown. The curves at threshold (blue and gold) exhibit a similar lag phase with timescales of N_b saturation corresponding to the timescales of array formation. The curve not at threshold (purple) does not have a significant lag phase and corresponds to a system that becomes kinetically trapped in an amorphous state.

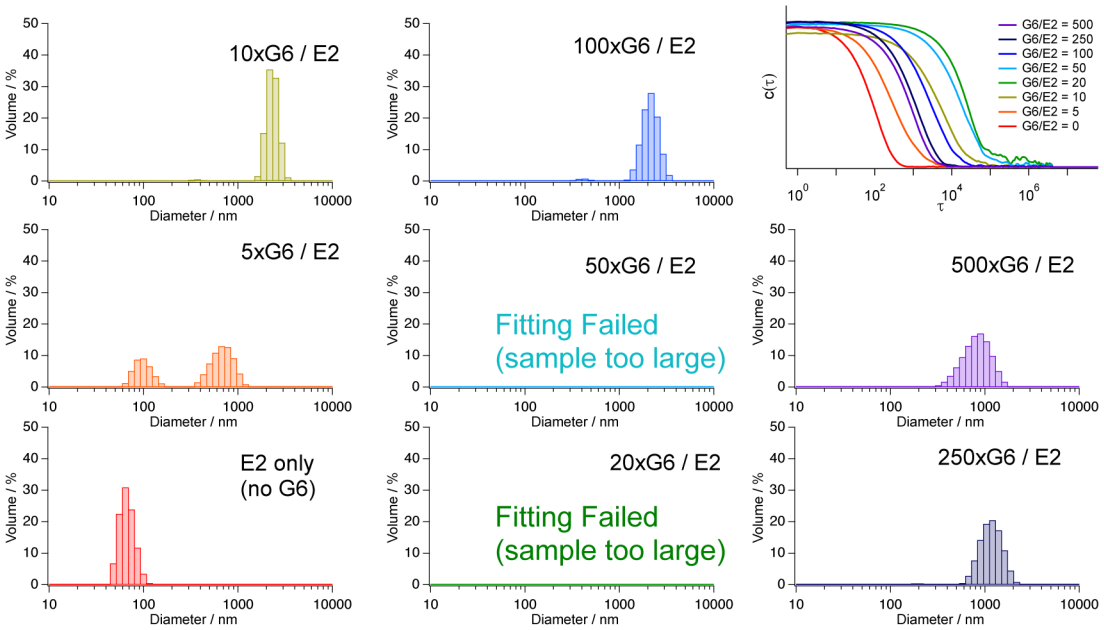

Figure S22: Correlation functions from dynamic light scattering measurements (top right), and corresponding volume-averaged hydrodynamic diameter distributions of P22-E2 VLPs mixed with G6 dendrimers at various concentrations c_d from 0 to 500 dendrimers per VLP in ionic strength of 10 mM (sodium phosphate 2.5 mM, sodium chloride 5 mM, pH 7.0). The size of the assembly increased with increasing c_d up to 50. At $c_d = 20$ and $c_d = 50$, fitting of the measured correlation function to obtain hydrodynamic size failed because the samples were too large. When c_d is increased further, the average size of the assembled arrays decreased to about 1 micrometers at $c_d = 500$.